Kuroshio surface water intrusion into the eastern part of the transition domain: its pathways and decadal variations

Takuro Matsuta[a], Humio Mitsudera[b], Toru Miyama[c], and Hiroyuki Tomita[a]

[a] *Faculty of Environmental Earth Science, Hokkaido University, Sapporo, Japan.*

[b] *Pan-Okhotsk Research Center, Institute of Low Temperature Science, Hokkaido University, Sapporo, Japan*

[c] *Application Laboratory, Japan Agency for Marine-Earth Science and Technology, Yokohama, Japan.*

Corresponding author: Takuro Matsuta, matsuta@ees.hokudai.ac.jp

ABSTRACT

The quasi-stationary jets, called "J1" and "J2" in the western North Pacific Ocean, transport the warm and salty waters originating from the Kuroshio and form the transition domain (TD) between the subtropical and subarctic features. Although previous studies have revealed the Kuroshio water pathways from the Kuroshio Extension to the western part of the TD through J1, the pathways to the eastern part of the TD (ETD) have not been revealed yet. We use the backward particle-tracking method to evaluate the Kuroshio water pathways from the Kuroshio Extension to the ETD. Our results identify that the Kuroshio Extension Northern Branch is the dominant pathway. The subarctic Front, the main jet of the Kuroshio Extension, and J1 also contribute to the Kuroshio water intrusion with the aid of eddy transports. We also find that the Kuroshio water intrusion affects the decadal sea surface temperature and surface heat flux variations. When the Kuroshio water intrusion is enhanced, the heat transport into the transition domain from the Kuroshio Extension and the heat release to the atmosphere from the transition domain are enhanced. The decadal variation of Kuroshio water intrusion correlates with the J2 strength and not with the Kuroshio Extension latitude. Using the Hilbert Empirical Orthogonal Function, we show that the remote force in the Gulf of Alaska and the central North Pacific Ocean possibly drives the decadal variation of J2 strength. In addition to this remote mechanism, the geostrophic anomalies forced by the local wind stress anomalies are also important.

Keywords:

Kuroshio Extension, Kuroshio water intrusion, eddy transport, North Pacific transition domain

Statements and Declarations

Competing Interests: Authors declare that they have no conflict of interest.

1. Introduction

There are two quasi-stationary jets that connect the subtropical and subarctic regions in the western North Pacific Ocean (see J1 and J2 in **Fig. 1a**) (Isoguchi et al. 2006; Wagawa et al. 2014; Mitsudera et al. 2018; Nishikawa et al. 2021). These jets transport relatively warm and salty surface waters from the Kuroshio; therefore, the sea surface temperature (SST) is relatively high near the jets (**Fig. 1b**). Because of this intermediate nature between the subtropical and subarctic regions, this area is called the Transition Domain (TD) (gray-shaded are in **Fig. 1a**). Numerical experiments and observations have suggested that the SST anomalies in the TD likely have significant impacts on extratropical atmospheric circulations (e.g., Tanimoto et al. 2003; Nakamura et al. 2004; Taguchi et al. 2009; Kwon et al. 2010; Taguchi et al. 2012; Ogawa et al. 2012; Ma et al. 2015, 2016; Qiu et al. 2021; Joh et al. 2023). In addition, the physical environment and food supply of this area are considered important for fisheries science (e.g., Oyaizu et al. 2022; Niu et al. 2024). For example, interannual variations in this area have been suggested to affect the squid catch (Niu et al. 2024). A comprehensive review of the hydrographic features of the Kuroshio-Oyashio region and their impacts on the atmosphere can be found in Kida et al. (2015).

Previous studies have suggested the dynamical link between the Kuroshio Extension (KE) region and the western part of TD (west of 160°E). Nishikawa et al. (2021) and Matsuta and Mitsudera (2023) showed that the time fluctuations of KE are essential for the transport of the Kuroshio water across the Subantarctic boundary (SAB) and reach the J1 entrance. They suggested that if the time fluctuations were absent, J1 would never contain the subtropical waters. In addition, the decadal variations of the KE latitude control the dynamical state of J1 (Wagawa et al. 2014; Qiu et al. 2017; Matsuta and Mitsudera 2023). Furthermore, the heat (Qiu et al. 2017; Miyama et al. 2021) and salinity (Kido et al. 2021) advections from the KE control the mixed layer condition of the western part of TD. These studies consistently suggest that the decadal variations of KE are responsible for the SST variations of TD.

By contrast, the dynamical link between the KE region and the eastern part of TD (ETD) is not well understood. In this study, the ETD is defined as the region of 165° E– 180°E, 41°N– 46°N. In particular, the pathways of the Kuroshio water into the ETD have not been revealed. Nishikawa et al. (2021) suspected that some J1 waters enter the ETD (we call this route *J1 route*, hereafter), but other routes were not investigated. Another candidate for Kuroshio water intrusion is J2. As shown in **Fig. 1**b, the SST is relatively high near J2, indicating that J2 transports the Kuroshio water into the ETD. We divide the J2 route into three candidates based on paths reaching J2. One candidate is the Kuroshio Extension Northern Branch (KENB) route (hereinafter referred to as *KENB route*). According to previous studies (e.g., Levine and White 1983; Mizuno and White 1983; Hurlburt and Metzger 1998; Sainz-Trapaga et al. 2001; Kida et al. 2015), the KE jet bifurcates around the Shatsky Rise at around 153°E (**Fig. 1c**) and the northern branch, i.e., KENB flows northeastward. Although the KENB has been recognized as a pathway of KE waters to the SAB (Kida et al. 2015), its link to the ETD via J2 has not been revealed yet. In addition, the SAB may be a possible route. Although the SAB works as a barrier for the Kuroshio water intrusion into J1 (Nishikawa et al. 2021; Matsuta and Mitsudera 2023), the eastward current associated with the SAB may transport Kuroshio water towards the entrance of J2, which was suspected in Nishikawa et al. (2021). We call this candidate *SAB route*, hereafter. The other candidate is a route via the main jet of KE downstream of 160°E connecting to J2. According to Chen et al. (2014b), the cross-stream eddy diffusivity is enhanced downstream of Shatsky Rise (**Fig. 1a**), which may allow the Kuroshio waters to escape from the KE jet and enter the ETD (hereinafter referred to as *KE-Eddy route*).

To address the Kuroshio water pathway into the ETD and evaluate the relative importance of the J1, KENB, SAB, and KE-Eddy routes, particle tracking is conducted in this study. From the particle trajectories, we quantify the relative contribution of the four candidates. In addition, we investigate the influence of the Kuroshio water intrusion on the surface thermal condition of the ETD. Although previous studies have shown that the oceanic processes control the SST of the Kuroshio-Oyashio region (e.g., Yasuda and Kitamura 2003; Tanimoto et al. 2003; Nonaka et al. 2006; Joh et al. 2023), the fine-scale structure within the TD, which influences the air-sea fluxes (Tomita et al. 2011; Takahashi et al. 2020), might have been overlooked; therefore, we revisit the local SST variations of ETD in the context of the Kuroshio water intrusion. Furthermore, we discuss possible mechanisms for decadal variabilities of Kuroshio water intrusion into the ETD based on the Hilbert Empirical Orthogonal Functions (HEOF) (Hannachi et al. 2007).

This manuscript is organized as follows. Section 2 provides a brief description of the dataset and particle-tracking method. We also introduce the HEOF in this section. In section 3, the Kuroshio water pathway into the ETD is explored. Section 4 investigates the correlation among the Kuroshio water intrusion, SST, and turbulent heat flux. We also discuss possible mechanisms of the decadal variations of the Kuroshio water intrusion into the ETD using the HEOF. Finally, a summary and discussion of the present study are given in section 5.

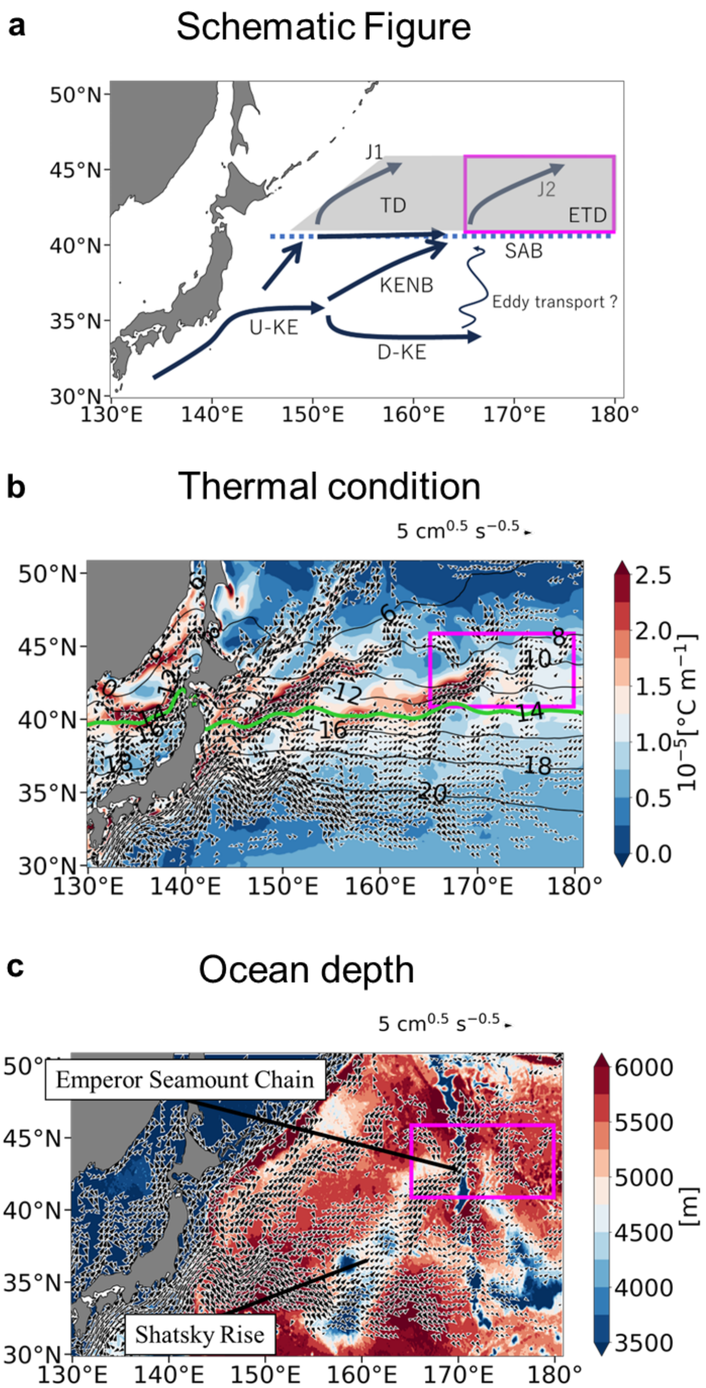

Fig. 1 a A schematic of our target region. The upstream and downstream region of KE is denoted by U-KE and D-KE. Two distinct northeastward jets north of SAB indicated by the blue dashed line are J1 and J2, and the northern branch of the KE downstream of 153°E is the KENB. The TD is gray-shaded. We mainly analyze the Kuroshio water intrusion into the ETD indicated by the magenta box. See the main text for detailed definitions. **b** SST gradient in $10^{-5}[°\mathrm{C\ m^{-1}}]$ obtained from observations between 1994 and 2022 (The descriptions of data sets are given in section 2.) Black contours represent the SST. Black arrows indicate the square-rooted horizontal geostrophic velocity $\left(\mathrm{sign}(u_g)\sqrt{|u_g|}, \mathrm{sign}(v_g)\sqrt{|v_g|}\right)$, where $\mathrm{sign}(X)$ returns the sign of X. Velocity vectors whose speeds are less than $5\ \mathrm{cm\ s^{-1}}$ are masked. The 14 °C contour indicated by green curve roughly follows the SAB. **c** Ocean depth data from the OCCAM project at the Southampton Oceanography Centre. The Shatsky Rise and the Emperor Seamount Chain are indicated. The black vectors are the same as those in the upper panel.

2. Data and Methods

2.1 Datasets

We used daily, absolute dynamic topography (ADT), zonal, and meridional geostrophic velocities derived from the Ssalto/Duacs delayed-time Level 4 sea surface height data. The Ssalto/Duacs altimeter products were manufactured and distributed by the Copernicus Marine Environment Monitoring Service (CMEMS) (https://marine.copernicus.eu/). The data period is from 1993 to 2022 and the spatial resolution is $0.25° \times 0.25°$. According to Nishikawa et al. (2021), the geostrophic velocity field from CMEMS well corresponds with the buoy moving released in the TD, and hence we considered using the geostrophic velocity to be reasonable in our target region.

The monthly SST, wind stress, and turbulent heat flux (the sum of the sensible and latent heat fluxes) with a spatial resolution of $0.25° \times 0.25°$ are obtained from the third-generation Japanese Ocean Flux Data Sets with Use of Remote-Sensing Observations (J-OFURO3). J-OFURO3 uses multi-satellite data for the estimation of each ocean surface flux parameter. The data period used in this study is 1993–2022. A detailed description of J-OFURO3 is found in Tomita et al. (2019).

In section 4, we discuss the relationship between the decadal variations of ADT and the two major modes, the Pacific Decadal Oscillation (PDO) (Mantua et al. 1997) and the North Pacific Gyre Oscillation (NPGO) (Di Lorenzo et al. 2008). According to Mantua et al. (1997), negative sea surface height anomalies are generated in the central North Pacific owing to the intensified Aleutian Low during the positive PDO phase, and the signals are reversed during the negative PDO phase. The annual mean of the PDO index is distributed by the Japan Meteorological Agency (https://www.data.jma.go.jp/kaiyou/data/shindan/b_1/pdo/annpdo.txt). On the other hand, according to Di Lorenzo et al. (2008), when the NPGO is in a positive phase, the sea level pressure is negative in the Gulf of Alaska and positive in the subtropical region. The signs are reversed during the negative NPGO phase. The monthly value of the NPGO index (Di Lorenzo et al. 2008) is from the NOAA/ESRL PSL webpage (https://www.psl.noaa.gov/gcos_wgsp/Timeseries/NPGO/) on 2024-10-07 and averaged annually.

2.2 Particle tracking

To investigate the surface water pathways into the ETD, we examine the particle tracking. Particle trajectories are governed by

$$\frac{d\mathbf{x}}{dt} = \mathbf{u}_g(\boldsymbol{x}, t), \tag{1}$$

where $\mathbf{x} = (x, y)$ is the position of each particle and $\mathbf{u}_g = (u_g, v_g)$ is the horizontal geostrophic velocity vector at the surface. The lefthand side of Eq. (1) is discretized by the fourth-order Runge Kutta method with an integration time-step of 3 hours. Because the temporal resolution of CMEMS data is daily, the velocity fields are interpolated linearly every 3 hours. Particles are located over the ETD with $0.25° \times 0.25°$ resolution and tracked backward for 360 days. Because the particle originating from the Kuroshio goes back to the Philippine Sea from the TD within one year (Nishikawa et al. 2021), the 360-day backward tracking is sufficient for identifying the Kuroshio water pathways. The initial time of the tracking is the first day of each month during 1994–2022, and thus 348 track datasets were available. For each track, the particle position is stored every day.

To quantify the Kuroshio water pathways into the ETD, we estimate the count function of particles. The count function is defined on the bins placed at $0.5° \times 0.5°$ intervals over the North Pacific Ocean. The count function, $F(B_i, t_n)$ counts the number of Kuroshio-origin trajectories that cross the bin B_i during the month, t_n:

$$F(B_i, t_n) = \sum_{p\text{: Kuroshio origin particle that enters the ETD on month } t_n} f(B_i; p), \tag{2}$$

where the "existence function" $f(B_i; p)$ is 1 if the particle p enters the bin B_i at least once during its trajectory and 0 otherwise. In this study, we regard particles originating south of 34°N as "Kuroshio-origin particles." As an example of the existence function, we show the first 10-day backward pathway started from the red rectangular box on 1995-08-01 (**Fig. 2**). The existence function $f(B_i; p)$ is 1 in the blue-colored bins. The count function is obtained by summing the existence function f over all the Kuroshio origin particles that enter the ETD in each month, t_n. Using the definition, we define the annually-averaged count function during 1994–2022 as

$$\overline{F}(B_i) = \frac{1}{29}\sum_{n=1}^{348} F(B_i, t_n), \tag{3}$$

which counts the number that B_i is included in the Kuroshio water intrusion pathways in a year. We briefly call the annually-averaged count function as "count function", hereafter. Since the count function has a large value along the preferred routes, the count function measures for each grid the likelihood of the Kuroshio water intrusion pathway.

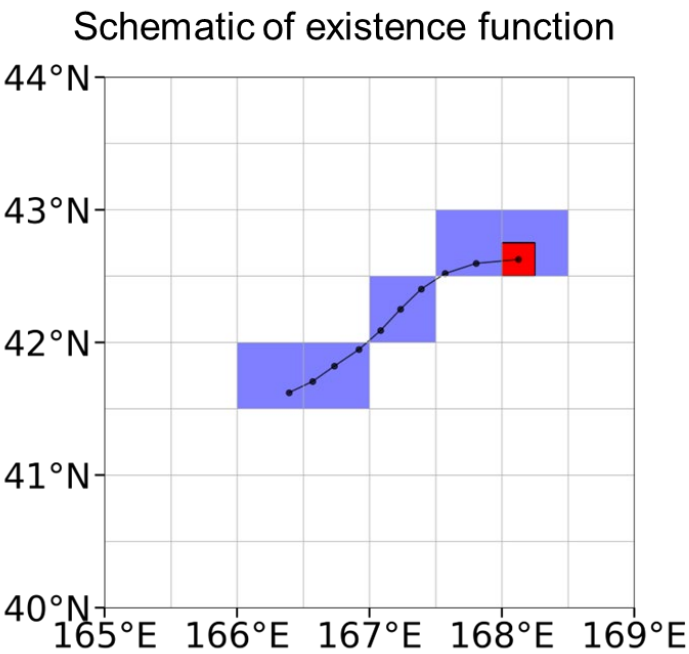

Fig. 2. Schematic of the "existence function," $f(B_i;p)$. The black line indicates the first 10-day trajectory starting from the red rectangular box on 1995-08-01 as an example. The function is 1 on the bins where the particle passes (indicated by blue color) and 0 otherwise.

2.3 A brief introduction to the HEOF analysis

To analyze the propagation of ADT anomalies, we conduct the HEOF analysis (e.g., Rasmusson et al. 1981; Barnett 1983; Horel 1984; Hannachi et al. 2007) in section 4. While the conventional empirical orthogonal function (EOF) analysis finds the stationary patterns, and thereby the propagating signals are not captured, the HEOF analysis identifies the propagating signals as modes. Although the Hovmöller diagram is usually utilized to discuss wave propagations, the HEOF is more suitable for understanding complex propagating wave paths, because the direction of wave propagation does not need to be determined in advance in the HEOF analysis. For conciseness, a detailed explanation of Hilbert EOF is provided in the Appendix.

It should be noted that eigenmodes obtained from the HEOF do not necessarily correspond one-to-one with the PDO and NPGO. This is because the PDO and NPGO are identified as stationary patterns by the conventional EOF and do not contain information on wave propagation associated with these modes. In our case, the PDO signals split into several HEOF modes as shown in Section 4.3.

3. Identification of Kuroshio water intrusion routes into the ETD

3.1. Routes of Kuroshio water intrusion into the ETD

From the annual averaged value of the count function of Kuroshio origin particles (**Fig. 3**), the most prominent pathway is found to be the KENB route indicated by the red contour. Qualitatively, the quasi-stationary KENB jet (see black arrows in **Fig. 3**) appears to directly transport the Kuroshio water into the entrance of J2 across the SAB at around (165°E, 40°N). To confirm this assumption, we show the individual Kuroshio water pathways. **Figure 4a** shows the backward trajectories of Kuroshio origin waters from April 2003 to March 2004 as an example. Here, to highlight representative trajectories, the trajectories that enter the small magenta box in **Fig. 4a** are shown instead of showing all trajectories towards the ETD. In this case, all the trajectories are along the KE jet in its upstream region (west of 150°E) since the cross-stream diffusivity is small in the upstream region of KE (Chen et al. 2014b). The pathways split into three groups downstream of Shatsky Rise. This feature is also consistent with the enhanced cross-stream eddy diffusivity suggested by Chen et al. (2014b). The first group (red trajectories) is trapped by the KENB and transported into the J2 entrance at around (165°E, 40°N), which corresponds to the KENB route.

The count function (**Fig. 3**) also has relatively high values between the red and cyan contours in **Fig. 3**. The northern part of the area is attributed to the particles that escape from the KENB on the way. The cyan trajectories in **Fig. 4a** illustrate this route. They escape from the KENB at its entrance at around (154°E, 38°N) and continue northward. At around 40°N, the SAB, which is indicated by the 14°C SST contour, blocks the northward flow to enter the subarctic region. This corresponds to the transport barrier identified by the Lagrangian coherent structure in Matsuta and Mitsudera (2023). The transport barrier associated with the SAB is also evident in the drifting buoys (Nishikawa et al. 2021). Finally, the trajectories confluence with the KENB route at the entrance of J2 at around 165° E. This route corresponds to the SAB route suggested by Nishikawa et al. (2021).

The southern part of the relatively high-count function area is attributed to the KE-Eddy route suggested in Section 1. According to **Fig. 4a**, the yellow trajectories south of 35°N travel eastward along the KE after passing the Shatsky Rise. At around 163°E, they escape from the KE against the mean flow. They turn northward and confluence with the KENB and SAB routes around the SAB.

The escapes from the KENB in the SAB route and from KE in the KE-Eddy route can be explained by eddy activities. Although the background field is relatively stable in the downstream region of KE than the upstream region, the transport of eddies enhances the eddy activities downstream of KE and affects the mean flow (Chen et al. 2014a,b; Aoki et al. 2016; Yang and Liang 2016; Matsuta and Masumoto 2021; Yang et al. 2021). **Figure 4b** shows the eddy kinetic energy averaged from March 2003 to March 2004. Here, the eddy velocity is defined as the anomaly from 45-day centered moving average velocity, i.e., 91-day lowpass filtered velocity. The transient eddy kinetic energy exceeds $3000\ \mathrm{cm^2\ s^{-2}}$ at the entrance of KENB ($152°\mathrm{E}, 37°\mathrm{N}$) and in the downstream region of KE ($163°\mathrm{E}, 34°\mathrm{N}$), which allows the surface waters to escape from the mean currents by the cross-stream eddy diffusivity (Chen et al. 2014b). The role of eddy transport is evaluated in the next section.

In addition to the KENB, SAB, and KE-Eddy routes, the J1 route (see the northern part of the black contour in **Fig. 3**) also contributes to the Kuroshio water intrusion, although the count function is approximately one-third of the values of the other routes. In this route, the Kuroshio waters once enter the subarctic region along the J1 and directly intrude into the northern part of the ETD, which is consistent with the results of Nishikawa et al. (2021).

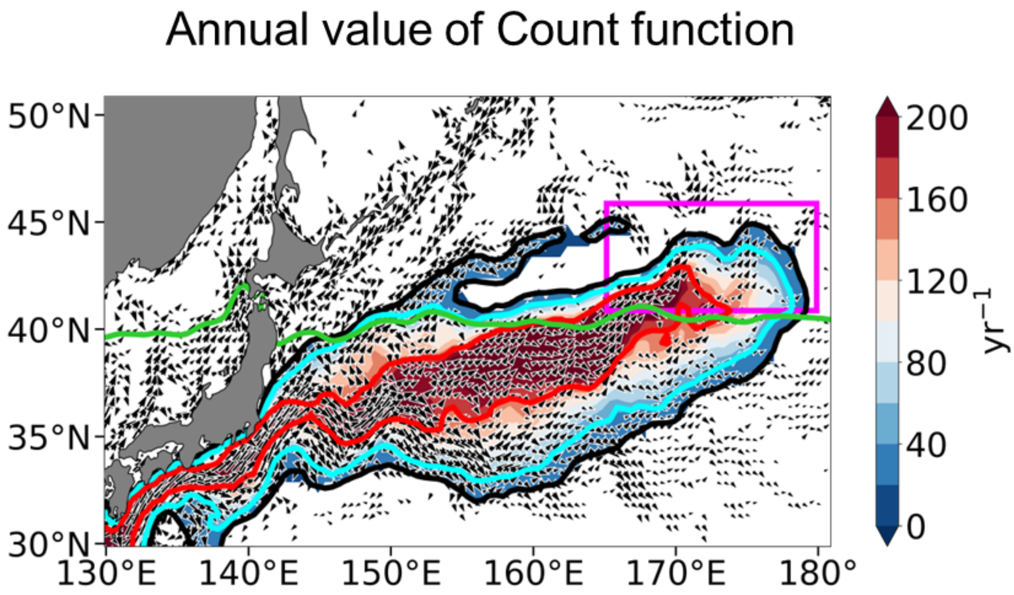

Fig. 3. Horizontal distribution of the count function of particles originating south of 34°N. Bins whose value is smaller than 15 are masked. The backward tracking starts from the ETD indicated by the magenta box. The black arrows and green contour are the same as those in **Fig. 1b**. The count function is greater than 160, 45, and 20 in the region encompassed by red, cyan, and black contours, respectively.

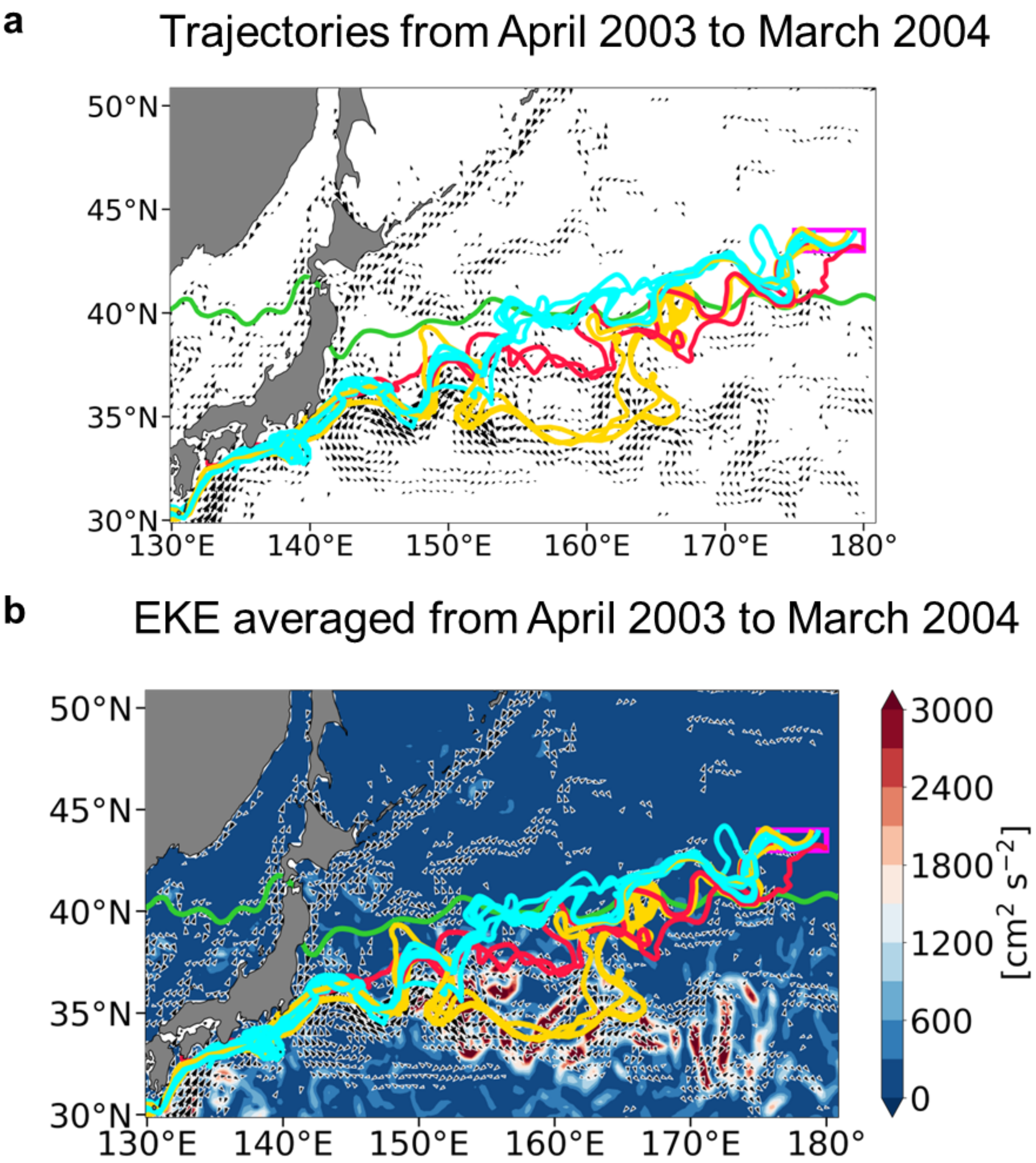

Fig. 4 a Color lines indicate the Kuroshio water pathway from April 2003 to March 2004 into the rectangular region included by magenta boxes (noting that this region is a subregion of ETD). Black arrows indicate the 45-day centered moving averaged square-rooted horizontal geostrophic velocity. Velocity vectors whose speeds are less than 10 cm s^{-1} are masked. The 14 °C SST contour indicated by the green curve roughly follows the SAB. The SST is averaged from April 2003 to March 2004. Red, cyan, and yellow trajectories correspond to the KENB, SAB, and KE-eddy routes (see the main text in detail.) **b** Same as the upper panel, but the eddy kinetic energy in [cm^2 s^{-2}] averaged from April 2003 to March 2004 is superimposed.

3.2. Contribution of eddies to the Kuroshio water intrusion

To highlight the eddy contribution to the Kuroshio water intrusion, we calculate the count function using 45- and 180-day centered moving averaged velocity fields in the same manner as $\overline{F}(B_i)$. We denote the former $\overline{F^{(45)}}(B_i)$ and the latter $\overline{F^{(180)}}(B_i)$. The 45-day centered moving average corresponds to the 91-day lowpass filter and thereby eliminates short-lived eddies. The 180-day centered moving average corresponds to the 361-day lowpass filter and thereby eliminates long-lived eddies as well as short-lived ones. The positive anomaly of the count function, $\overline{F}(B_i)$ from $\overline{F^{(45)}}(B_i)$ emphasizes the contribution of temporal fluctuations shorter than 91 days, while the positive anomaly of the count function, $\overline{F}(B_i)$ from $\overline{F^{(180)}}(B_i)$ emphasizes the contribution of time fluctuations shorter than 361 days.

According to **Fig. 5a**, the ratio of count function anomalies from $\overline{F^{(45)}}(B_i)$ show positive values over the Kuroshio-Oyashio region. In particular, the ratio of the anomaly is nearly 60 % along the KE-Eddy route (the region of $155°\text{E} - 165°\text{E}$, $33°\text{N} - 36°\text{N}$), indicating that eddies are responsible for the KE-Eddy route. The anomalies also reach 40 % north of the SAB, indicating that the eddies allow the Kuroshio waters to escape from the KENB and enter the SAB route. In addition, the anomalies exceed 40 % along J1. Because the fluctuations shorter than 91 days enhance the Kuroshio water intrusion into J1 (Matsuta and Mitsudera 2023), the inflow of Kuroshio waters from J1 to the ETD consequently increases by the short-time fluctuations.

The count function anomalies from $\overline{F^{(180)}}(B_i)$ are also investigated (**Fig. 5b**). The horizontal distribution of anomalies is similar to the former case, but the positive anomalies increase. The anomalies are more than 80 % along the KE-Eddy, SAB, and J1 routes, indicating that both the short-lived and long-lived eddies are responsible for these routes. Furthermore, the anomalies also become evident along the KENB in this case. Positive anomalies become evident in the southern part of KENB (the region of $157°\text{E} - 165°\text{E}$, $36°\text{N} - 38°\text{N}$), while the anomaly has small negative values along the KENB core. These changes indicate that the fluctuations along the KENB widen the KENB route.

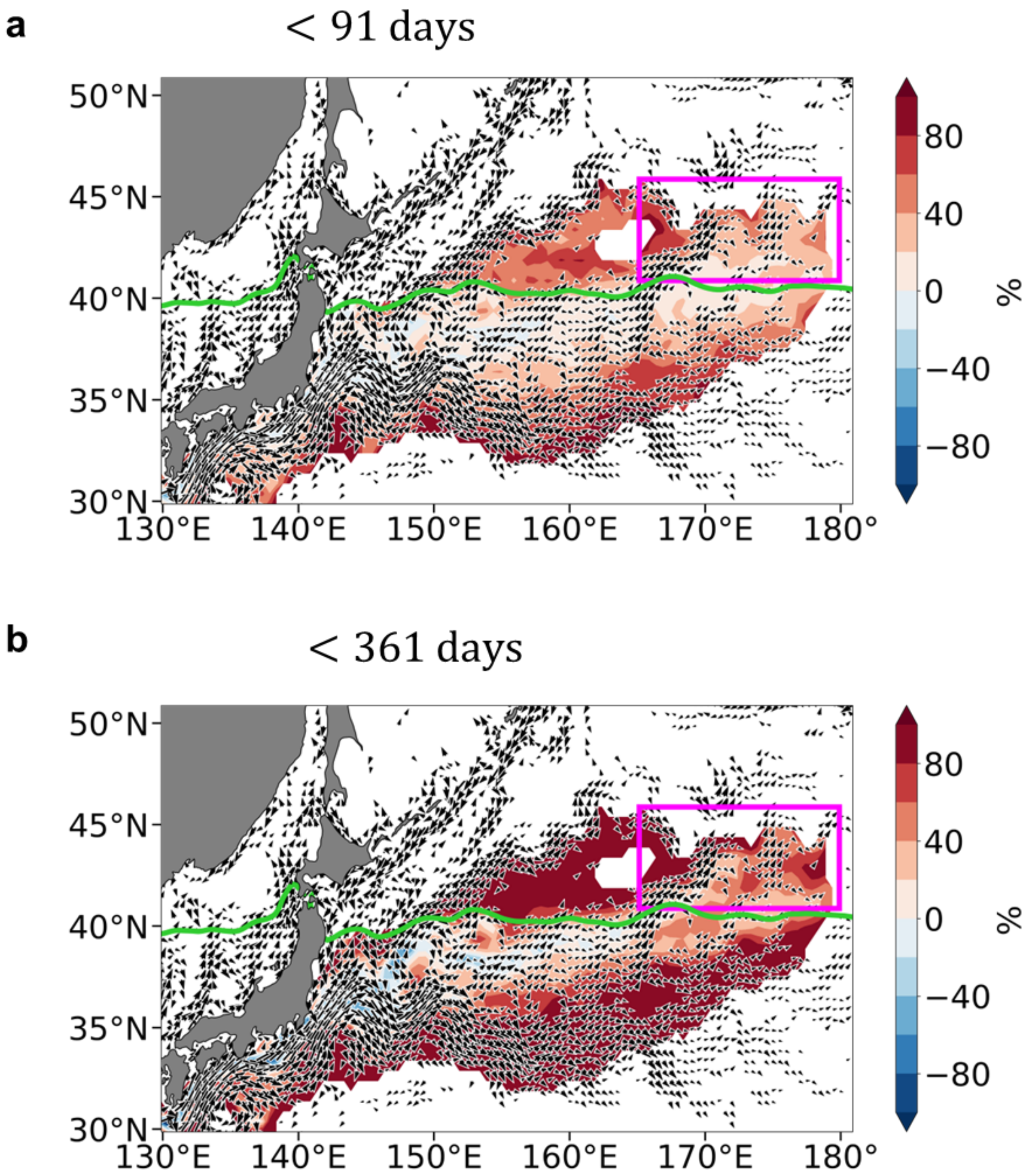

Fig. 5. Color shades denote **a** $100(\overline{F}(B_i) - \overline{F^{(45)}}(B_i))\,/\overline{F}(B_i)$ and **b** $100(\overline{F}(B_i) - \overline{F^{(180)}}(B_i))/\overline{F}(B_i)$. Here, we indicate the annual averaging of each count function by $\overline{\cdot}$. The region where the count function $\overline{F}(B_i)$ is smaller than 10 is masked. The black arrows, green contour, and rectangular box are the same as those in **Fig. 1b**.

4. Decadal variations of the Kuroshio water intrusion and its impact on the thermal condition of the ocean surface

4.1 Relationship between the Kuroshio water intrusion and ocean surface thermal conditions in the ETD

We discuss the relationship between the Kuroshio water intrusion into the ETD and surface thermal conditions in the ETD. To quantify the time series of the Kuroshio water intrusion, we count the number of Kuroshio origin trajectories, i.e., originating from south of 34°N over the ETD (**Fig. 1a**) and define it as the "Kuroshio water intrusion number," N_{J2}. **Figure 6a** shows the time series of the N_{J2} anomaly and domain-averaged SST anomaly over the ETD. Each time series is normalized by its standard deviation and annually averaged. The SST of the ETD and N_{J2} show the decadal variations. For example, N_{J2} appear to be one cycle during 1994–2010. The correlation coefficient between them is 0.65 with a p-value of $\sim 10^{-4}$ during 1994–2020, suggesting that the heat transport by the Kuroshio water intrusion affects the SST in the ETD. The correlation coefficient between the turbulent heat flux (upward positive) averaged in the same region and N_{J2} (**Fig. 6b**) is consistently 0.61 with a p-value of $\sim 10^{-4}$ during 1994–2020, suggesting that the heat transported by the Kuroshio water intrusion is released to the atmosphere. Therefore, the Kuroshio water intrusion is likely to regulate the surface condition of ETD and possibly force the overlying atmosphere (e.g., Tanimoto et al. 2003; Nakamura et al. 2004; Xie 2004; Sugimoto 2014).

Before this section ends, the abrupt warming after 2021 should be noted. In this period, the Kuroshio water intrusion cannot explain the SST and heat flux anomalies (**Fig. 6**). As shown in **Fig. 7a**, the SST anomalies in 2022 cover the subarctic region. Similar sudden warmings are also evident over the globe in 2022 (Storto and Yang 2024). Consistent with the abrupt SST increase over the North Pacific Ocean, the anomalies of air temperature at 10 m height are positive over the region of positive SST anomalies (**Fig.** 7b). Since the turbulent heat flux anomaly in 2022 is extremely positive i.e., upward (**Fig. 6b**), the SST anomalies are not owing to the heat flux into the ocean. Rather, the ocean is likely to warm the air temperature. The mechanism of the abrupt warming in 2022 is beyond the scope of this work but should be discussed in future work.

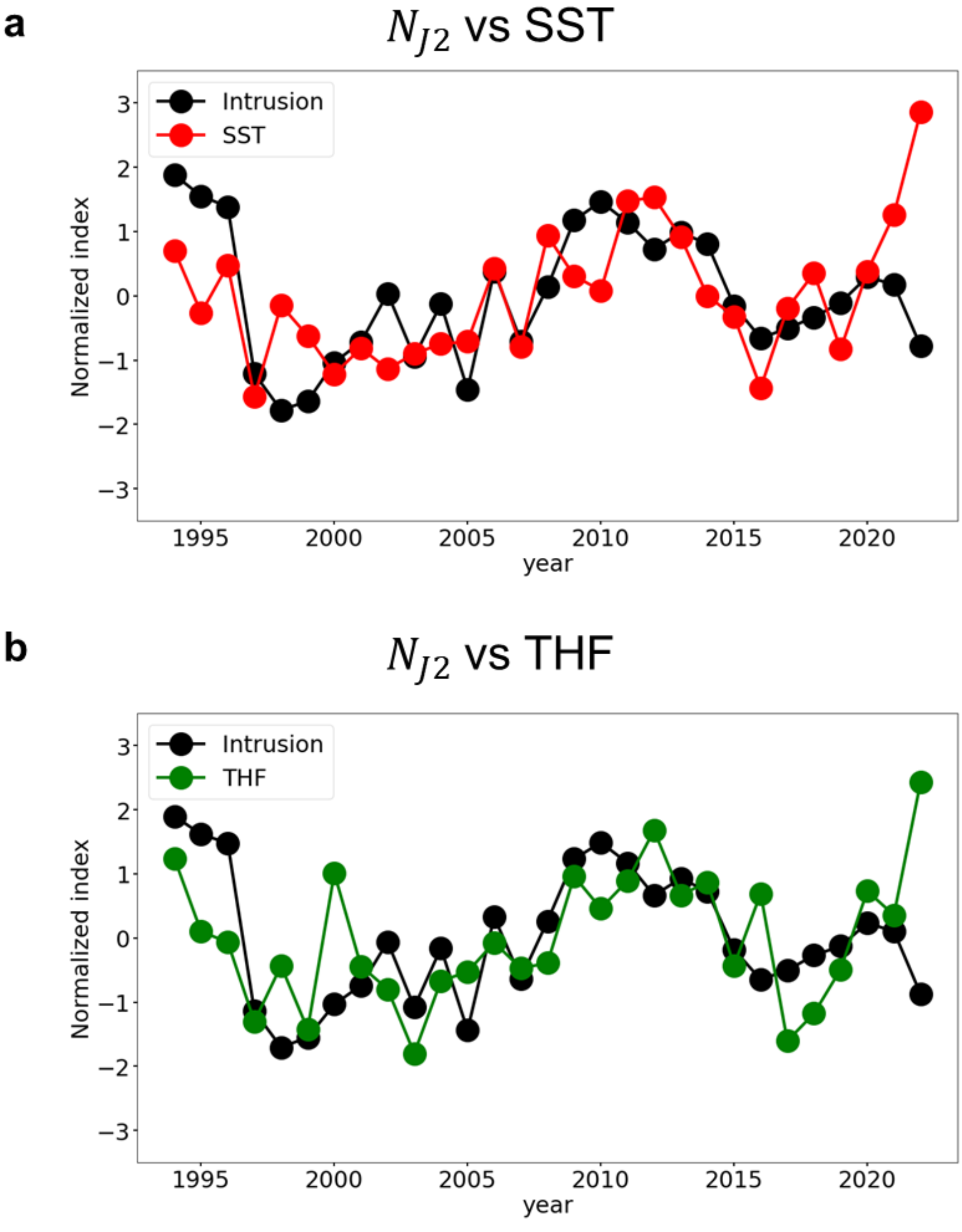

Fig. 6 **a** Annual averaged value of the Kuroshio water intrusion number, N_{J2}, (black curve) and domain-averaged SST (red curve) from 1994 to 2022. Each time series is normalized by its standard deviation. **b** Same as the upper panel but the green curve is for the turbulent heat flux. Positive values indicate the heat supply from the ocean to the atmosphere.

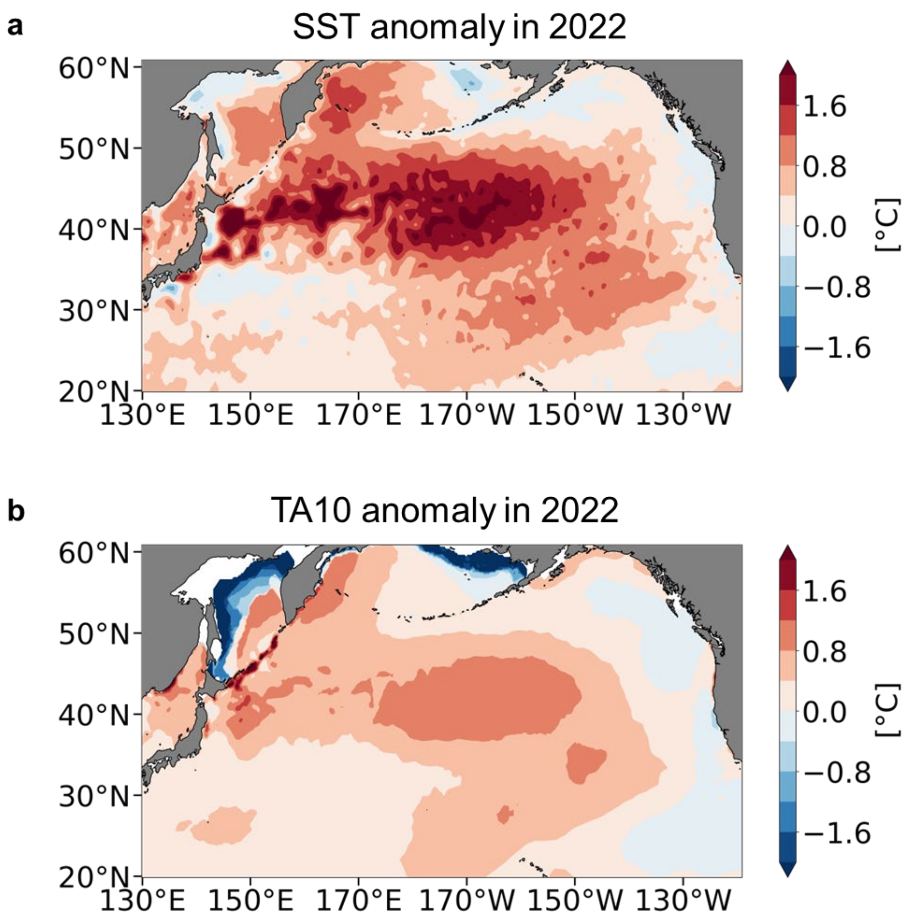

Fig. 7. **a** SST anomalies in 2022 from the mean SST during the period of 1994–2022. **b** Same as the upper panel but for air temperature at 10 m height.

4.2 Decadal variation of Kuroshio water intrusion into the ETD

To investigate possible mechanisms of decadal variations of Kuroshio water intrusion, we first analyze the relationship of N_{J2} with the J2 strength and the dynamical state of KE. We define the strength of J2 as the flow speed of northeastward flow averaged over the ETD, and we consider the meridional position of KE latitude as a proxy of the KE dynamical state following previous studies (e.g., Taguchi et al. 2007; Qiu and Chen 2010; Sugimoto 2014). Here, the KE latitude is defined as the latitude of the maximum speed between 30°N and 40°N, and averaged 143°E and 155°E as is done in Matsuta and Mitsudera (2023). Although the definition of KE latitude focuses on the upstream region of KE, the principle component for the conventional EOF first mode of the ADT over the Kuroshio-Oyashio region (130°E–180°E, 30°N–51°N) agrees with the KE latitude variation: the correlation coefficient between them is 0.92 with p-value of $\sim 10^{-12}$, and therefore the KE latitude reflects the dynamical states over the Kuroshio-Oyashio region.

The strength of the northeastward flow over the ETD correlates well with N_{J2} as shown in **Fig. 8a**. The correlation coefficient reaches 0.67 with a p-value of $\sim 10^{-5}$ during 1994–2020. By contrast, we do not find a clear relationship between KE latitude and N_{J2} (**Fig. 8b**), while the KE latitude affects the Kuroshio water intrusion into J1 (Wagawa et al. 2014; Matsuta and Mitsudera 2023). In fact, the correlation coefficient is only -0.07 with p-value of 0.73. Even if the correlation is calculated between 1994 and 2011, the correlation coefficient remains -0.16, indicating the bad correlation is not due to the analyzed period. Although the dynamical state of KE influences the turbulent heat flux over the KENB (Sugimoto 2014), the surface condition of the ETD is not directly connected with the KE region. Rather, our results suggest that J2 variations are more important. The discrepancy between our findings and Sugimoto (2014) may be attributed to the transport barrier imposed by the SAB. Since the Kuroshio waters cannot intrude into the TD across the SAB without the deformation of the SAB (Matsuta and Mitsudera 2023), the ETD is not always connected with the KE.

To reveal how the J2 strength variates, we conduct the composite analysis of the ADT anomalies over the North Pacific Ocean for three periods. The first period is 1994–1996, the second period is 1997–2000, and the third period is 2009–2011. The Kuroshio water intrusion, N_{J2} is greater than 1.0 standard deviation during the first and third periods, and lower than –1.0 standard deviation during the second period. Although N_{J2} is also lower than -1 standard deviation in 2003 and 2005, we do not analyze these years because the time series of N_{J2} variate interannually rather than decadal during 2003–2007. While the ADT has a positive trend over the North Pacific Ocean in these decades (Yang et al. 2020; Kawakami et al. 2023), the Kuroshio water intrusion does not show a significant trend, and thereby we analyze the detrended ADT and wind stress during 1994–2022 to focus on the decadal variations. The ADT anomalies from the average of detrended ADT values are referred to as "ADT anomaly" for simplicity if nothing is stated. In addition, we decompose the ETD region into two parts. The right triangular half of the ETD, along the diagonal drawn from the upper right to the lower left, is referred to as 'R-ETD', and the left triangular half along the same diagonal is referred to as 'L-ETD'.

During the first period (**Fig. 9a)**, the positive anomalies extend in a southwest direction from the Gulf of Alaska towards $(150°\mathrm{E}, 35°\mathrm{N})$. The positive anomalies overlap with the R-ETD. At the same time, the negative ADT anomalies are also evident in the region of $150°$ E– $180°\mathrm{E}$, $42°\mathrm{N}$– $50°$N, and overlap with the L-ETD. These ADT anomalies correspond to the increased northeastward geostrophic flow, i.e., the intensification of J2. In the second period (**Fig. 9b**), the positive anomalies located in the Gulf of Alaska during the first period appear to move southwestward and overlap with the L-ETD, which is evident in the movie for the ADT anomalies (see Online **Movie 1** in Supplementary Information). In addition, the negative anomalies are located in the R-ETD, although the amplitude is smaller than that of the positive anomalies in the L-ETD. These positive and negative anomalies form the ADT gradients favorable for the southwestward geostrophic current in the ETD, i.e., the J2 deceleration.

By contrast, the horizontal distribution of ADT anomalies during the third period is different from those in the former periods (**Fig. 9c**). The ADT anomalies in the third period are positive over the region of $160°$ E– $170°\mathrm{W}$, $30°\mathrm{N}$– $42°\mathrm{N}$. The positive anomalies slant northeastward and overlap with the R-ETD, which is favorable for the J2 intensification. In this period, the ADT anomalies are not remotely generated but formed locally (see **Movie 1** in Supplementary Information).

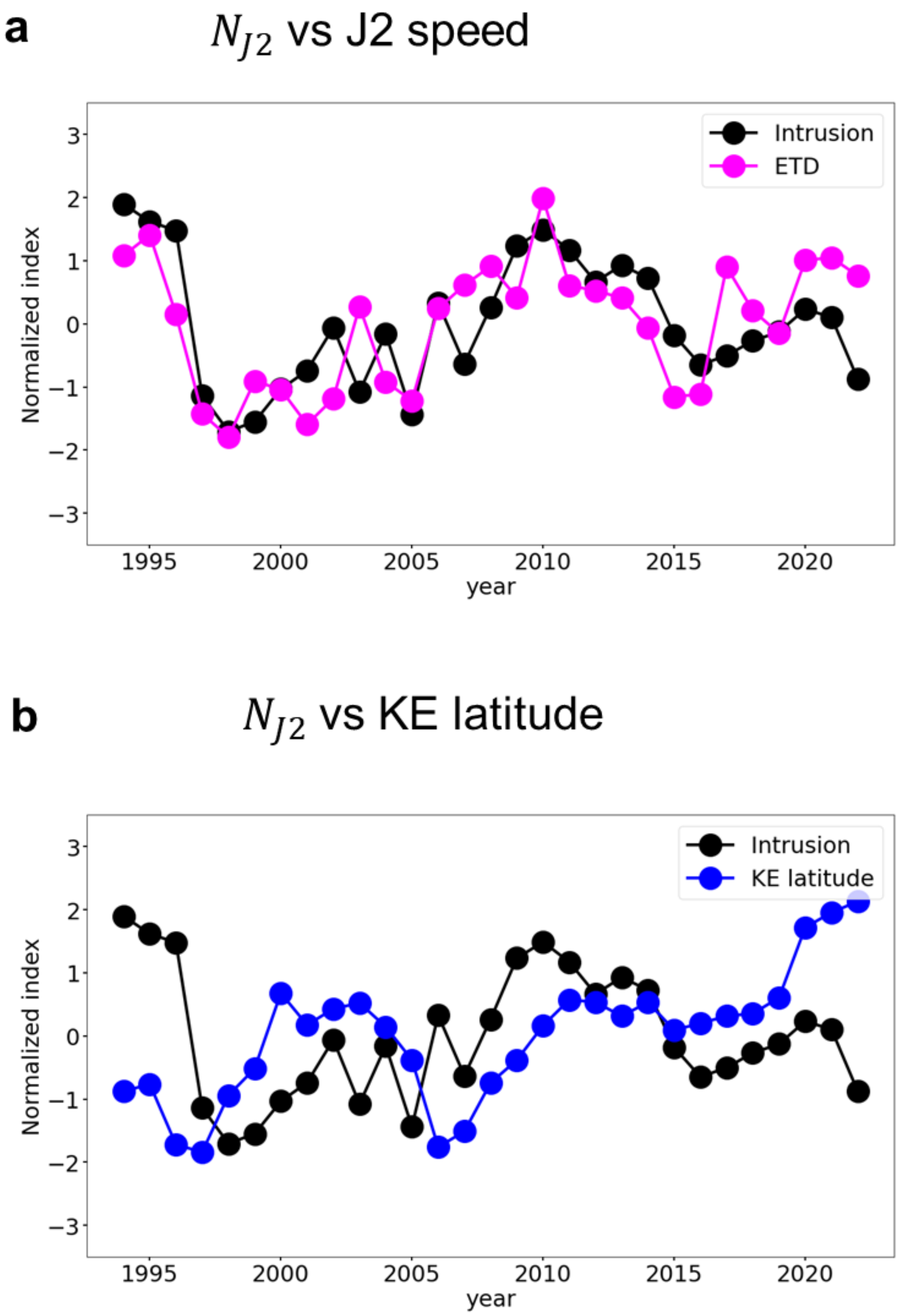

Fig. 8 **a** Magenta curve indicates the annual averaged value of the current speed of northeastward flow averaged over the ETD. **b** Blue curve indicates the KE latitude. Positive values of the KE latitude indicate the northward shift of KE. Black curve in each panel is the same as that in **Fig. 6a**.

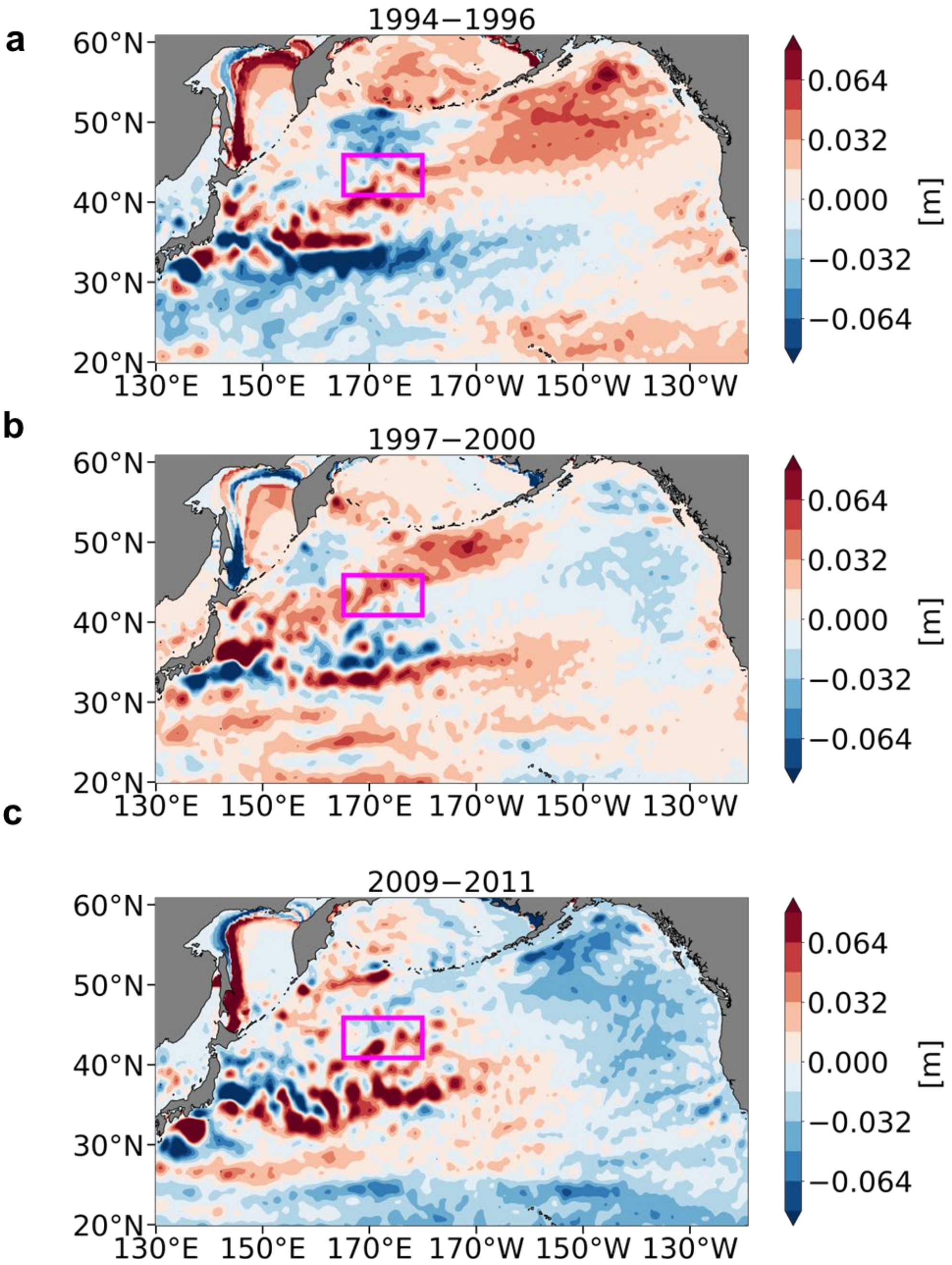

Fig. 9 ADT anomaly in [m] averaged during **a** 1994–1996, **b** 1997–2000, and **c** 2009–2011. The magenta boxes indicate the ETD.

4.3. Origin of ADT anomalies around the ETD identified by the HEOF analysis

To find the origins of the ADT anomalies associated with the J2 strength variations, we conduct the HEOF analysis for the monthly value of detrended ADT anomalies. Here, the monthly values are obtained by the monthly averaging of 361-day lowpass filtered daily ADT data as in Section 3.2 and detrended. The HEOF is conducted for the region of $130°\mathrm{E}-121°\mathrm{W}, 20°\mathrm{N}-61°\mathrm{N}$. Here, the analyzed period is $1994–2015$ to focus on the ADT anomalies associated with the three periods discussed in Section 4.2. The spatial amplitude, spatial relative phase, temporal amplitude, and temporal phase for the first, second, and third modes are shown in **Fig. 10**, **Fig. 11**, and **Fig. 12**, respectively. The first, second, and third modes explain the 26 %, 16 %, and 13 % of the ADT variations.

4.3.1 A DESCRIPTION OF HEOF MODES

Before discussing the ADT anomalies associated with the HEOF modes, we briefly describe each HEOF mode in this subsection. In the first mode, the large amplitude is located in the longitudinal band between $30°\mathrm{N}$ and $40°\mathrm{N}$ and the band extending from the Gulf of Alaska towards the ETD (**Fig. 10a**). Focusing on the spatial relative phase (**Fig. 10b**), it can be seen that the relative phase increases along the Alaska Peninsula (see the black arrow in **Fig. 10b**). The phase is around 72° at the eastern boundary of the Gulf of Alaska, and increase to $-36°$, i.e., $396°$ at around $(170°\mathrm{E}, 47°\mathrm{N})$. The temporal amplitude (**Fig. 10c**) is relatively large between 1994 and 2005, and the temporal phase variates by nearly $360°$. Therefore, the first mode corresponds to the propagation of the ADT anomalies from the Gulf of Alaska to the ETD during $1994–2005$. This point is confirmed in the next subsection.

The spatial amplitude of the second mode (**Fig. 11a**) is also high in the ETD, indicating that this mode also has the potential to affect the Kuroshio water intrusion. The spatial phase (**Fig. 11b**) slants northeastward from the ETD towards $(150°\mathrm{W}, 50°\mathrm{N})$, which possibly reflects the westward propagation of the baroclinic Rossby wave (see the black arrow in **Fig. 11b**). The northeastward slanting of the isophase line is probably explained by the phase speed difference of the baroclinic Rossby wave. According to FIG.7 of Qiu (2003), the first baroclinic Rossby wave phase speed at $40°\mathrm{N}$ is $0.02\ \mathrm{cm\ s^{-1}}$, while the speed is $0.01\ \mathrm{cm\ s^{-1}}$ at $46°\mathrm{N}$, which leads to the northward slanting of the isophase lines. According to **Fig. 11c**, the second mode explains the ADT anomalies for the period $1997–2002$, while the amplitude is relatively small during the first and third periods. We also find that the frequency of the mode is approximately 7 years at least before 2002 (**Fig. 11d**).

According to **Fig. 12a**, the spatial amplitude of the third mode is high south of the R-ETD, which is a similar pattern of the ADT anomalies during the third period (**Fig. 9c**). Consistently, the temporal amplitude has its maximum around 2010 (**Fig. 12c**), suggesting that the third mode is responsible for the ADT anomalies during the third period. This point is confirmed in the next subsection. The spatial phase in the region of $160°\mathrm{E} - 170°\mathrm{W}$, $35°\mathrm{N} - 45°\mathrm{N}$ is nearly equal except for the mesoscale noises (**Fig. 12b**), indicating that this mode does not correspond to the wave propagations but is generated locally, unlike the first and second modes. The temporal phase (**Fig. 12d**) indicates that the frequency of this mode is decadal after 2005. Although the frequency is approximately 5 years before 2005, the value of frequency has no physical meaning when the amplitude is small (Barnett 1983).

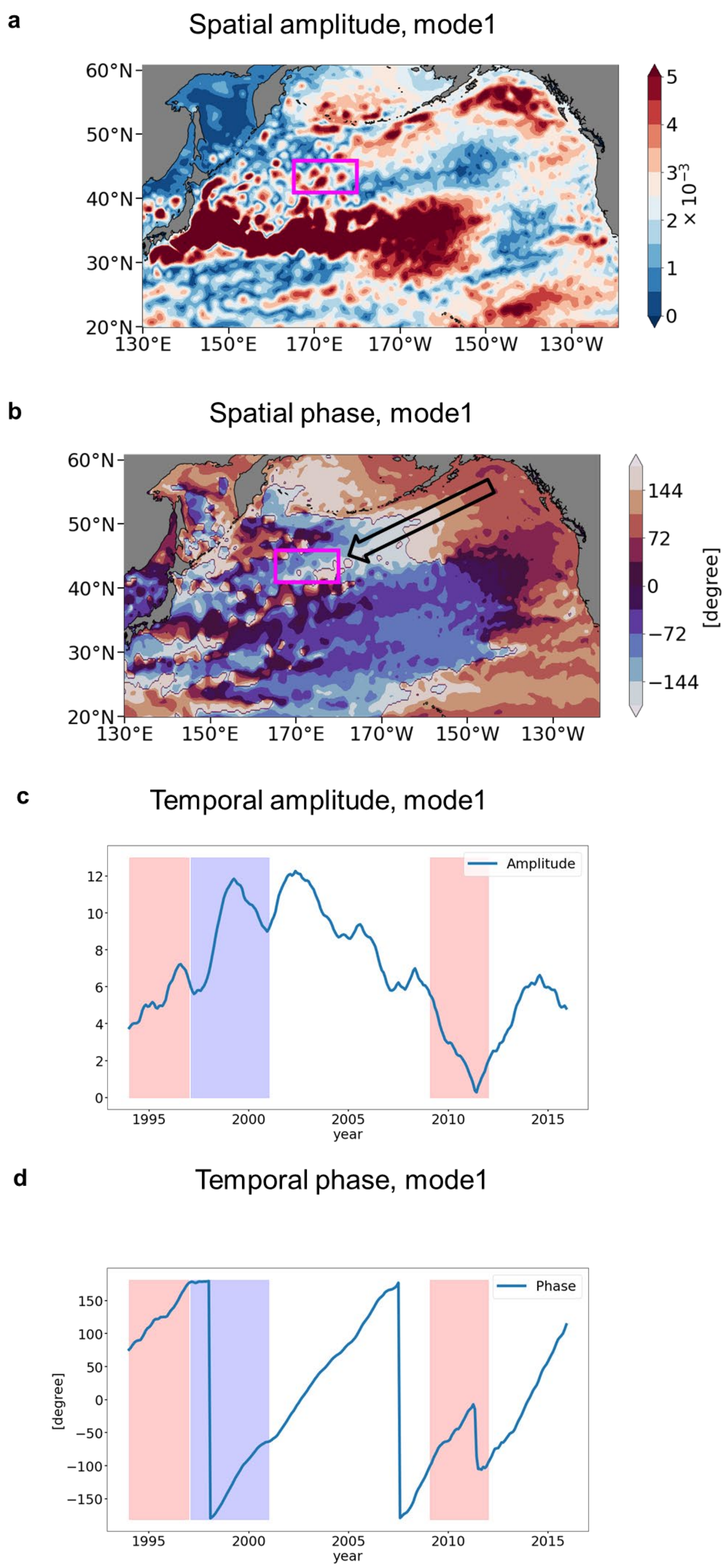

Fig. 10 a Horizontal distribution of spatial amplitude, **b** spatial relative phase, **c** temporal amplitude, and **d** temporal phase of the HEOF first mode. The black arrow in **b** indicates the wave propagation we focus on in the main text. The first and third periods are indicated by the red shaded areas and the second period is indicated by the blue shaded area.

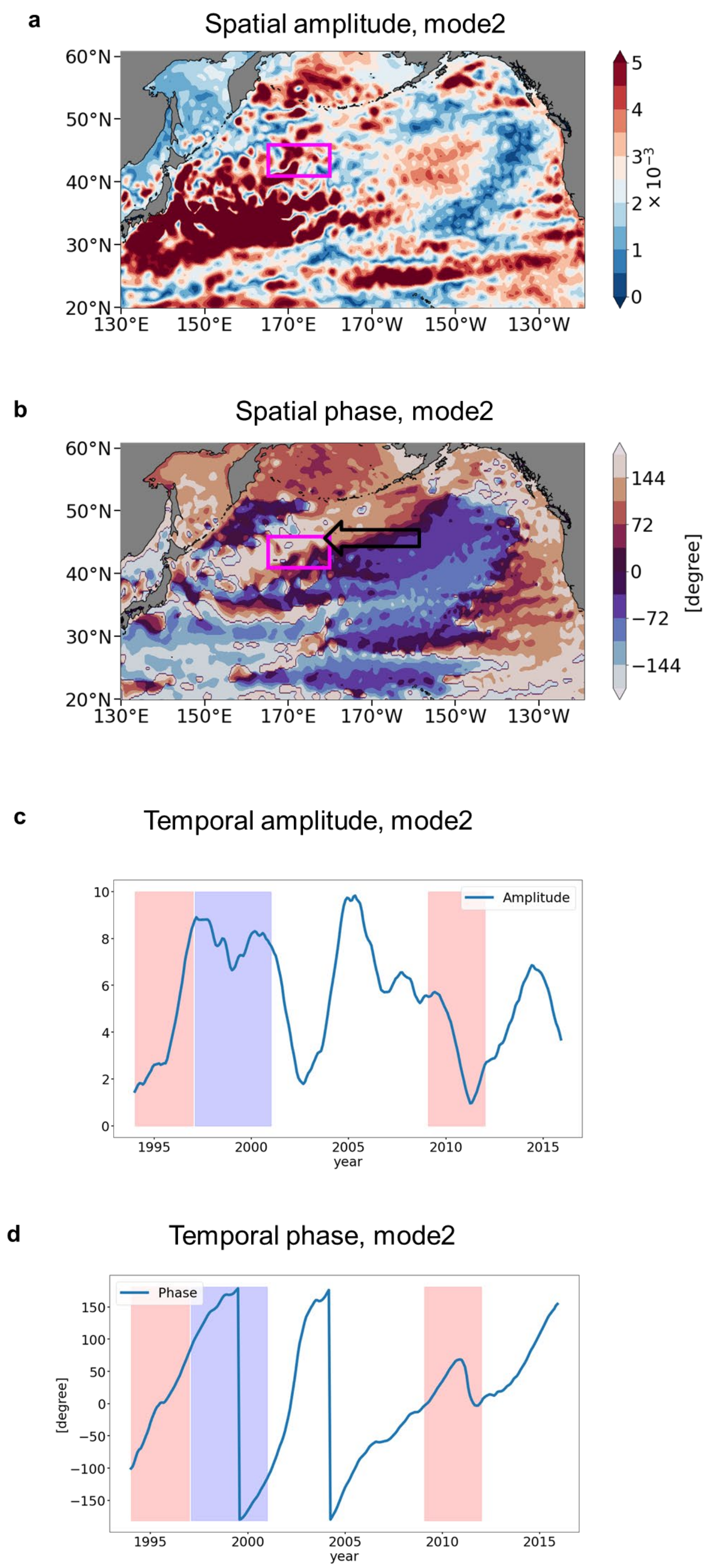

Fig. 11 Same as **Fig. 10** but for the HEOF second mode. The black arrow in **b** indicates the wave propagation we focus on in the main text.

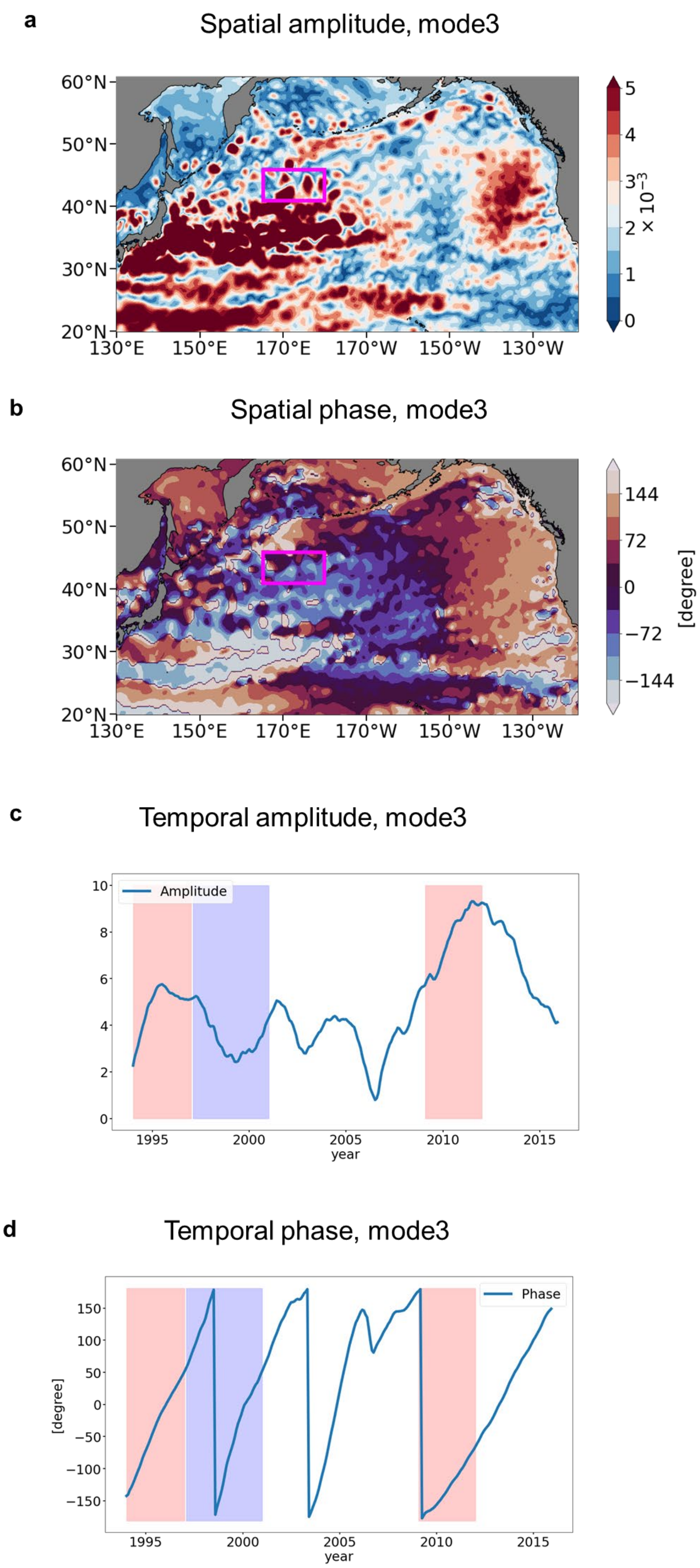

571

572 **Fig. 12** Same as **Fig. 10** but for the HEOF third mode.

4.3.2 RECONSTRUCTION OF THE ADT ANOMALIES FROM EACH MODE

In this subsection, we show that the ADT anomalies associated with the first and second modes are responsible for the J2 deceleration during the second period, while the third mode is responsible for the J2 acceleration during the third period (**Figs. 13−15**). We do not discuss the origins of ADT anomalies during the first period because there is no ADT data before 1993. Although we only display the reconstructed fields relevant to the ADT anomalies of the second and third periods in the main text, animations of reconstructed ADT fields during 1994‐2015 from each HEOF mode are provided in Supplementary Information (**Movie 2–4**).

The ADT anomalies reconstructed from the first mode are shown in **Fig. 13** from 1995 to 2000. Each value is annually averaged. There are negative ADT anomalies centered at $(165°\mathrm{W}, 35°\mathrm{N})$ and positive anomalies in the northern part of the Gulf of Alaska in 1995 and 1996. The positive anomalies propagate southwestward along the Alaska Peninsula during 1995‐1998 and reach the L-ETD in 1999 and 2000. As a result, this wave-like signal forms the favorable condition for the J2 deceleration in 1999 and 2000. This positive ADT anomaly band over the L-ETD is consistent with the ADT anomalies averaged during the second period (**Fig. 9b**). In addition to the remote effect, the local ADT anomalies are also found in the R-ETD. The positive ADT anomaly seen in the R-ETD in 1995 (**Fig. 13a**) is enhanced during the period of 1996‐1998 (**Fig. 13**b−d). Although we cannot discuss the formation mechanism of this localized signal since the data before 1993 is absent, the localized ADT anomalies are likely to influence the J2 strength with an aid of the propagating ADT anomalies from the Gulf of Alaska.

It should be noted that the ADT propagation speed is consistent with the spatial and temporal phases of the first mode. Noting that the spatial phase difference between Alaska Peninsula (108°) and the eastern part of ETD (−108°) is 144°. Since the frequency of the first mode is 10 year, the spatial phase difference corresponds to $10\ \mathrm{year} \times 144°/360° = 4.0\ \mathrm{year}$.

We also show the ADT anomalies reconstructed from the second mode in **Fig. 14**. In 1995 and 1996, there are small positive anomalies in the R-ETD, which corresponds to the ADT anomalies during the first period. The negative ADT anomalies are formed in the region of $170°\,\mathrm{E}{-}150°\mathrm{W},\ 35°\mathrm{N}{-}50°\mathrm{N}$ from 1996 to 1998, which propagate westward during 1997‐2000 and overlaps with the R-ETD in this period. Consistent with the spatial phase of the second mode (**Fig. 11b**), the propagation speed is faster in the lower latitude. In addition, the positive anomalies are formed in the L-ETD from 1997 to 2000.

Combining the reconstructed ADT anomalies from the first and second modes, we can interpret the origins of the ADT anomalies during the second period. In 1997 and 1998, there are positive ADT anomalies over the ETD due to the local enhancement and propagation from the Gulf of Alaska (see **Fig. 13c & d**). These anomalies alone are insufficient to explain the composite of ADT anomalies during 1997–2000 (**Fig. 9b**). Since the negative ADT anomalies from the central North Pacific due to the second mode (**Fig. 14c & d**) cancel the positive anomalies of the first mode in the R-ETD, the combination of the first and second modes (**Fig. 16**) is positive in the L-ETD and negative in the R-ETD, which is the favorable condition of the J2 deceleration. These structures are consistent with the ADT anomalies during the second period (**Fig. 9b**). In 1999 and 2000, both the first and second modes form positive anomalies in the L-ETD and negative anomalies in the R-ETD. In this sense, the ADT anomalies during the second period are formed by the two different remote processes with the aid of some local processes reflected in the first and second modes, respectively.

On the other hand, the positive ADT anomalies over the R-ETD during the third period (**Fig. 9c**) are formed by a local process. The ADT anomalies reconstructed from the third mode are shown in **Fig. 15**. In 2008, there are no positive anomalies around the ETD. The positive anomalies emerge in 2009 in the region of $170°\mathrm{E}–170°\mathrm{W}$, $35°\mathrm{N}–45°\mathrm{N}$, and expand in the region of $160°\mathrm{E}–150°\mathrm{W}$, $30°\mathrm{N}–50°\mathrm{N}$ from 2010 to 2012. The stationary pattern only overlaps with the R-ETD and does not overlap the L-ETD, resulting in the J2 acceleration. The shape of the positive anomalies in the reconstructed field is consistent with that in the third period (**Fig. 9c**). Unlike the first and second modes, the positive anomalies do not propagate, and thereby we conclude the J2 is locally accelerated during the third period.

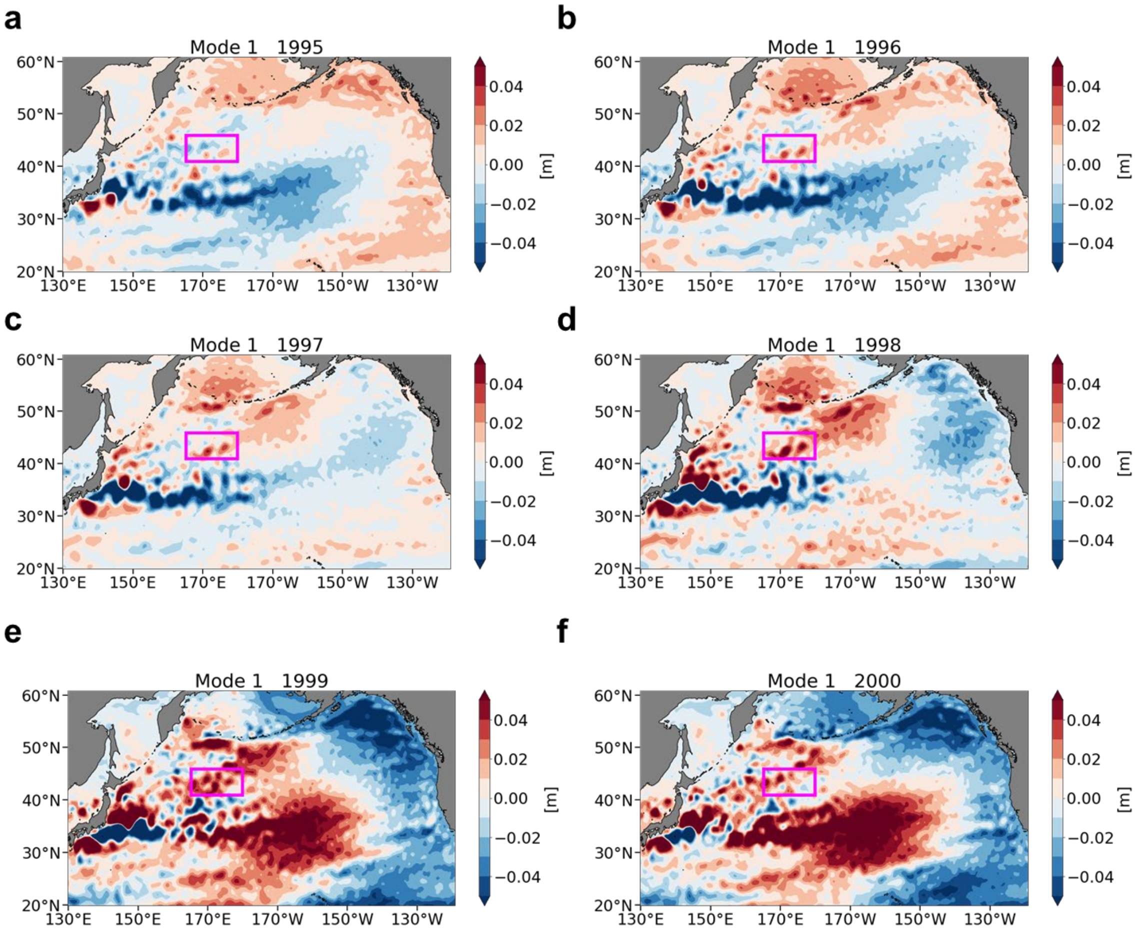

Fig. 13 Reconstructed ADT anomalies from the first mode averaged in **a** 1995, **b** 1996, **c**, 1997, **d** 1998, **e**, 1999, and **f** 2000.

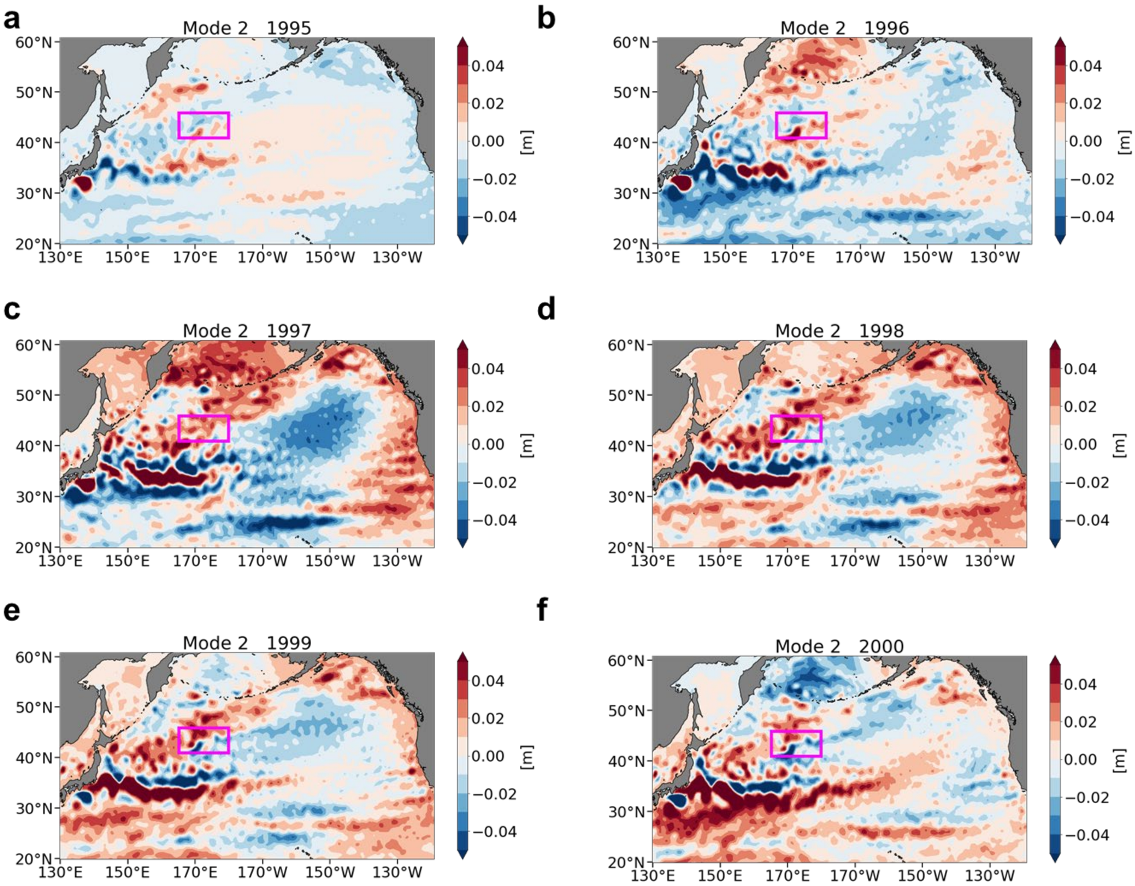

Fig. 14 Same as **Fig. 13** but reconstructed from the second mode.

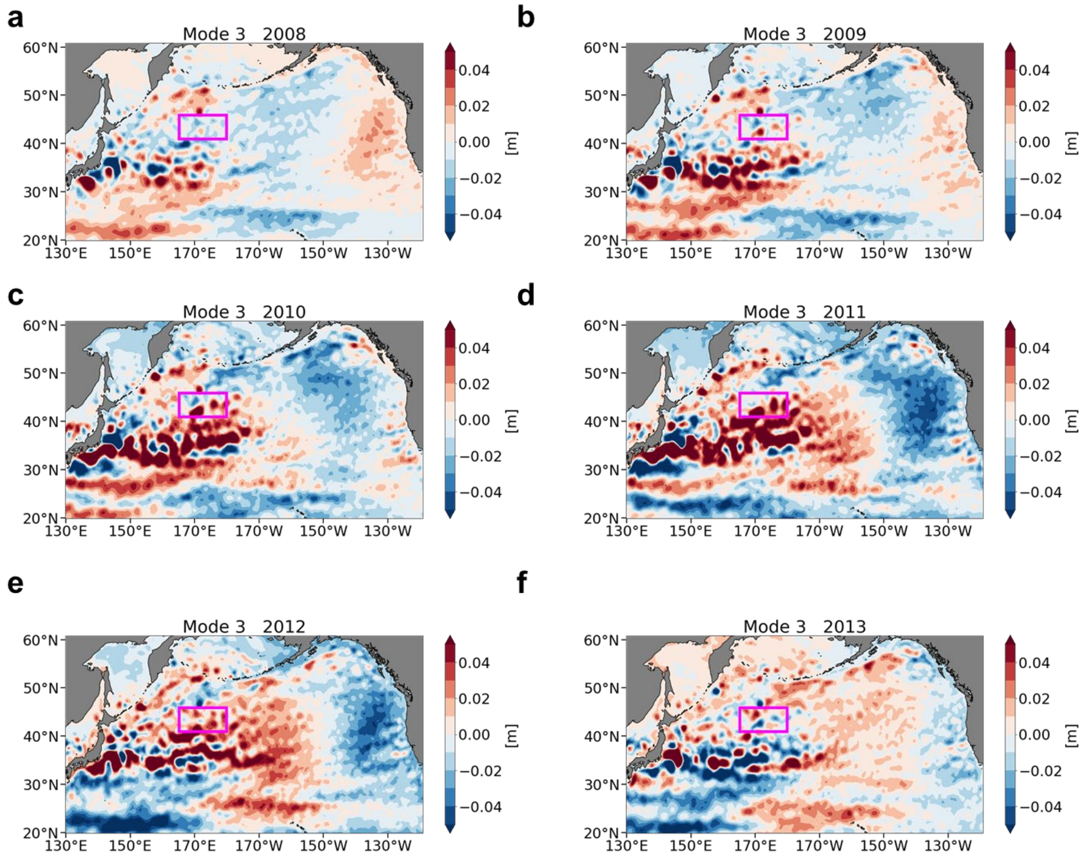

Fig. 15 Reconstructed ADT anomalies from the third mode averaged in **a** 2008, **b** 2009, **c** 2010, **d** 2011, **e**, 2012, and **f** 2013.

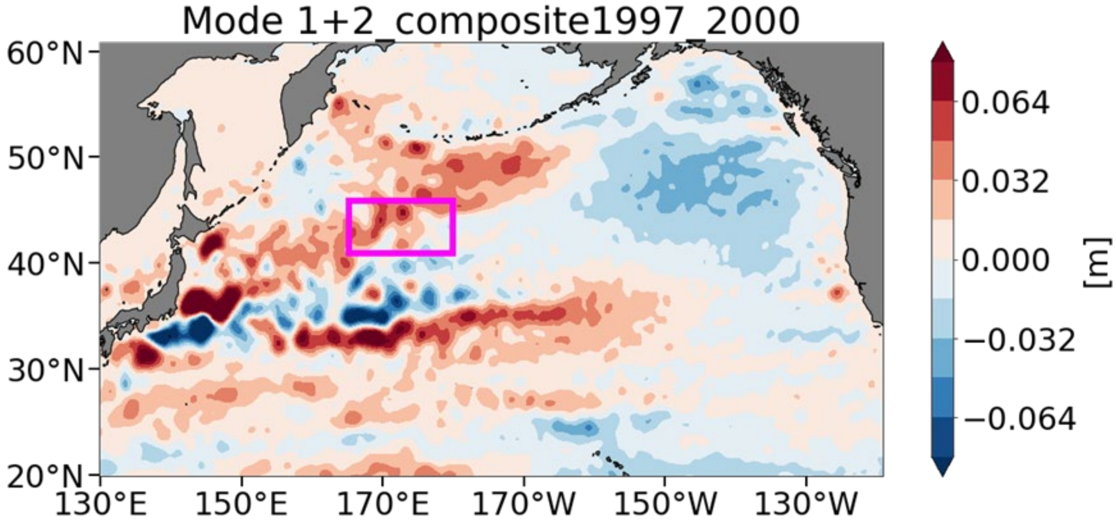

Fig. 16 The sum of ADT anomalies reconstructed from the first and second modes. Values are averaged between 1997 and 2000.

4.3.3 A POSSIBLE INTERPRETATION OF THE HEOF MODES

We discuss the relationship between the HEOF modes and the NPGO and PDO. In 1995 and 1996, the ADT anomalies associated with the first mode are negative in the central North Pacific Ocean and positive in the Gulf of Alaska as seen in **Fig. 13a** & **b**. This dipole pattern is consistent with the sign-reversed pattern of the NPGO (**Fig. 17a**), although the amplitude of the Gulf of Alaska is small in the reconstructed field. Consistently, the NPGO index is negative in these years (**Fig. 17b**). In addition, the positive anomalies in the central North Pacific Ocean and negative anomalies in the Gulf of Alaska from 1998 to 2000 (**Fig. 13d**-**f**) are consistent with the positive phase of NPGO (**Fig. 17b**), suggesting that the first mode reflects the ADT anomalies forced by the wind stress anomalies associated with the NPGO at least during 1995-2000.

On the other hand, the negative ADT anomalies reconstructed from the second mode are likely to be attributed to the intensified Aleutian Low during the positive PDO from 1997 to 2000. As shown in **Fig. 18a**, the ADT anomalies forced by the intensified Aleutian Low are located around (160°W, 35°N), which is consistent with the negative ADT anomalies shown in **Fig. 14b**-**d**. The PDO index is consistently in the positive phase in 1995-1998. Combining these arguments, we suggest that the J2 deceleration during the second period is remotely forced by both the negative NPGO pattern from 1994 to 1996 and positive PDO pattern from 1995 to 1997 through wave propagation.

In the third period, the positive anomalies are located in the central North Pacific Ocean as discussed in the previous subsection. The spatial pattern of the reconstructed ADT anomalies from the third mode is similar to the sign-reversed pattern of the PDO (**Fig. 18a**). The PDO index is in the negative phase (**Fig. 18b**) in this period, which also suggests that wind stress curl anomalies forced the J2 acceleration in this period. Although the center of positive anomaly is associated with the PDO located east of the ETD (**Fig. 18a**), the anomaly center overlaps with the ETD in the third period as seen in **Fig. 15c**-**e**, and hence the PDO locally affects the J2 strength in the this period. We summarize the J2 acceleration and deceleration mechanisms inferred from the case studies in the schematic figures of **Fig. 19**.

Before closing this section, it should be noted that the relationship of the J2 strength with the PDO and NPGO is not simple. Although the negative NPGO around 2005 results in southwestward propagation of positive ADT anomalies from the Gulf of Alaska during 2005–

2010 as in the 1990s, the amplitudes become very small before reaching the ETD (see **Movie 02** in Supplementary Information). As a result, the local mechanism of PDO is dominant and the remote mechanism of NPGO fails during the third period as seen in the previous paragraph. We thus suggest that both the NPGO and PDO patterns have the potential to influence the strength of J2, but not necessarily. Indeed, the relationship of N_{J2} with the PDO and NPGO appear to depend on the period (**Fig. 17b**, **Fig. 18b**).

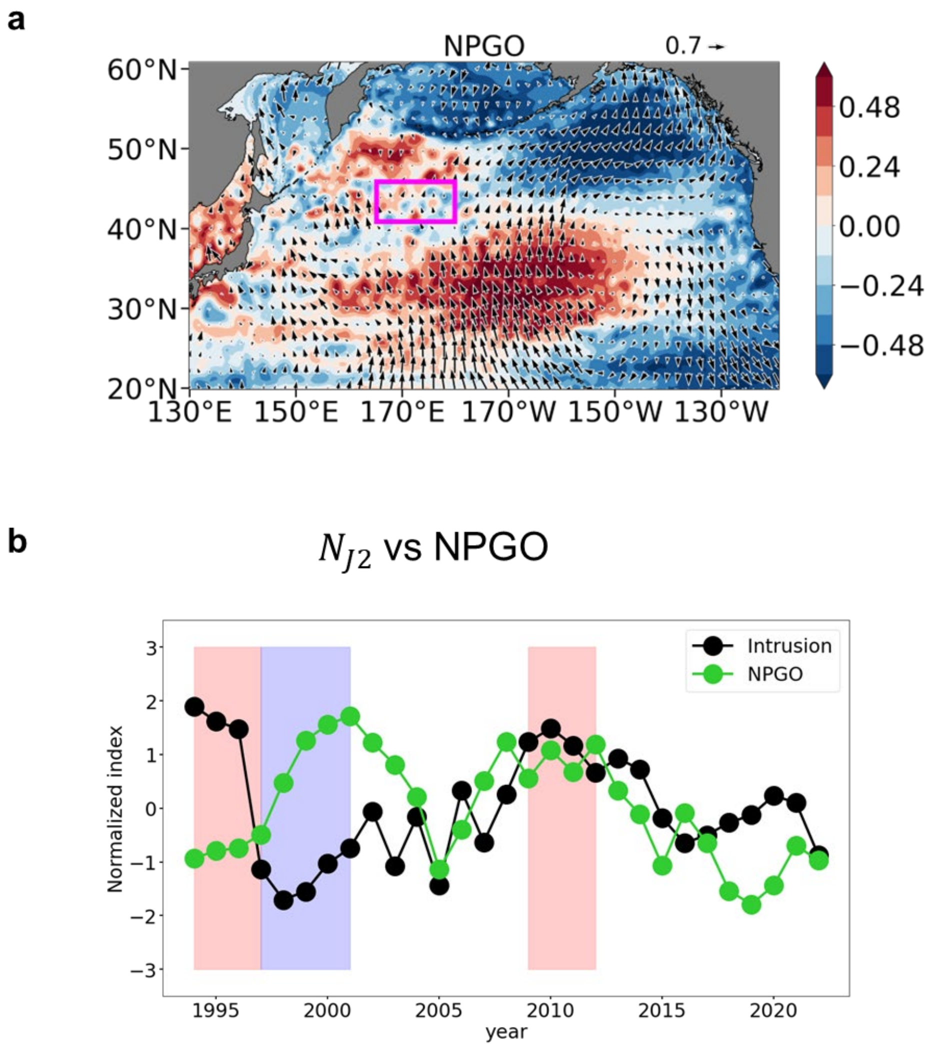

Fig. 17 **a** Simultaneous correlation of the ADT anomaly with the time series of the NPGO index. Vectors indicate the correlation of the wind stress vectors with the time series of the NPGO index. The magenta box indicates the ETD. **b** Lime green curve indicates the annual averaged value of the NPGO index. Black curve in each panel is the same as that in **Fig. 6a**. The first and third periods are indicated by the red shaded areas and the second period is indicated by the blue shaded area.

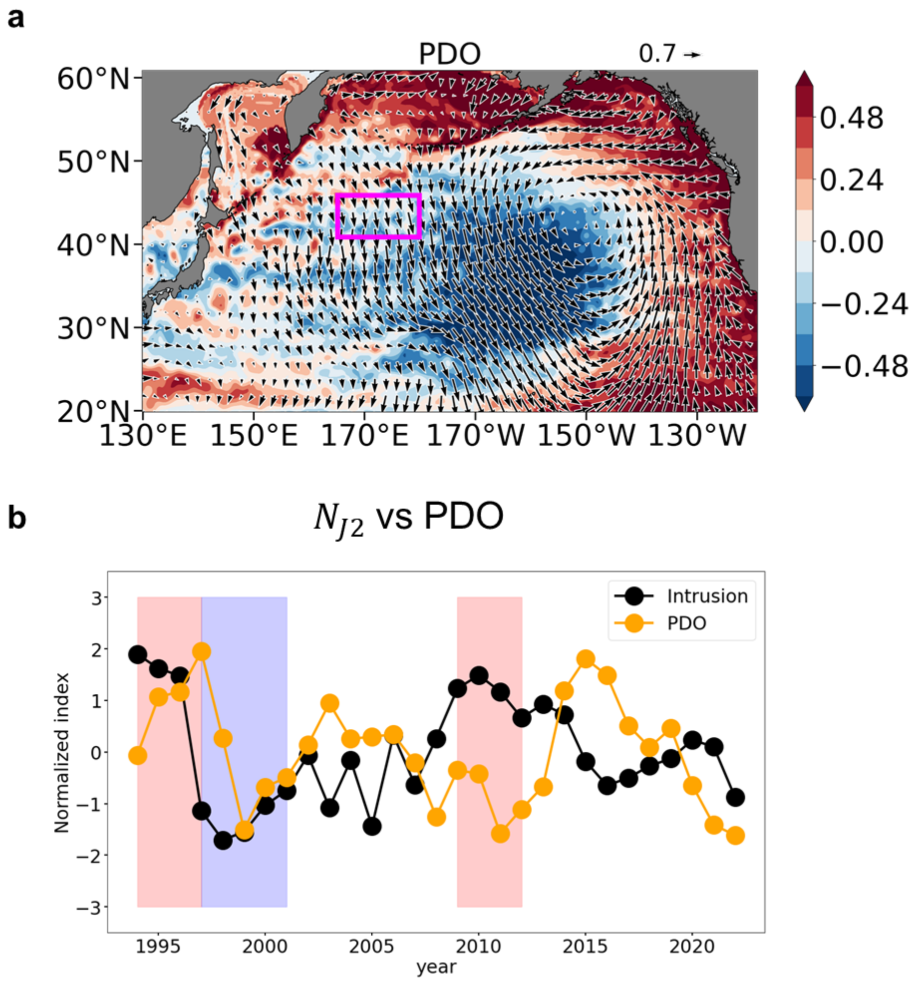

Fig. 18 a Simultaneous correlation of the ADT anomaly with the time series of the PDO index. Vectors indicate the correlation of the wind stress vectors with the time series of the PDO index. The magenta box indicates the ETD. **b** Yellow curve indicates the annual averaged value of the PDO index. Black curve in each panel is the same as that in **Fig. 6a**. The first and third periods are indicated by the red shaded areas and the second period is indicated by the blue shaded area.

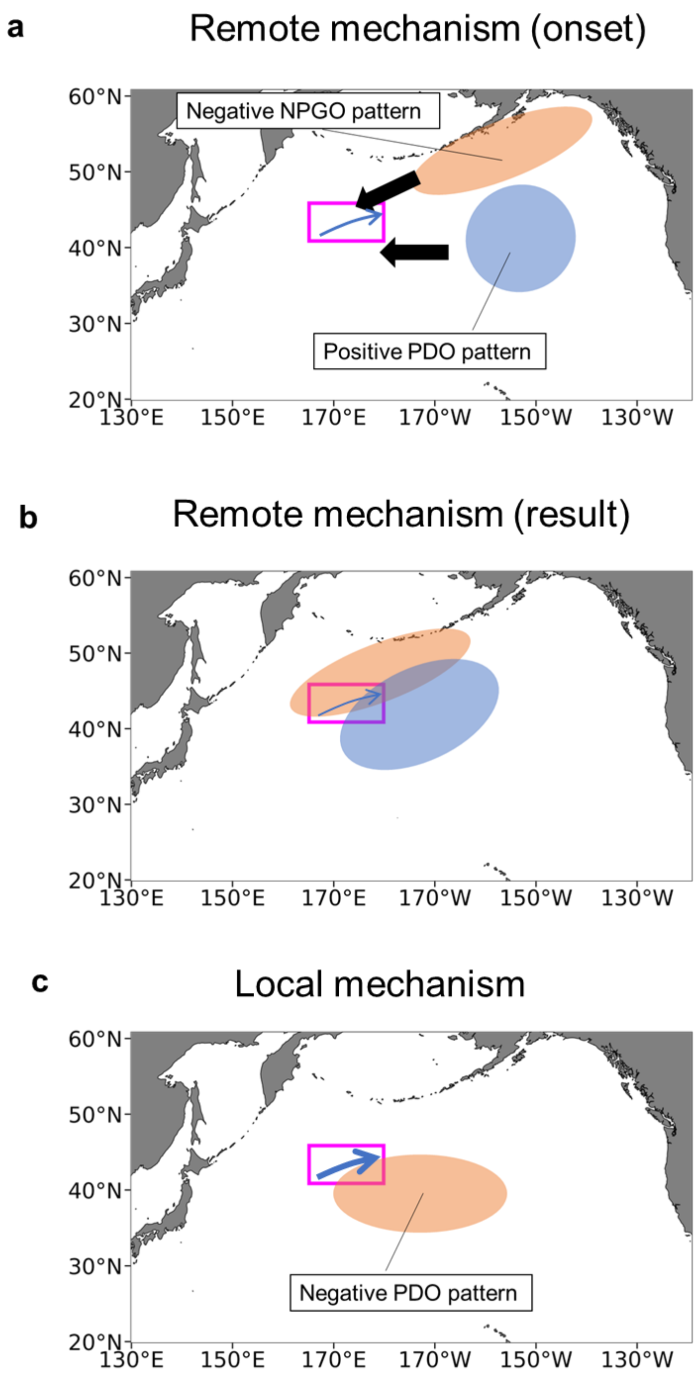

Fig. 19 Schematic for the J2 acceleration/deceleration by the remote and local mechanisms. **a** At the onset of the remote mechanism, the positive ADT anomalies are formed in the Gulf of Alaska. These anomalies propagate southwestward along the Alaska Peninsula as indicated by the black arrows. At the same time, the negative ADT anomalies associated with the positive PDO are formed in the central North Pacific Ocean, which propagates westward. Blue northeastward allow indicates the J2. **b** The southwestward propagation from the Gulf of Alaska tends to form the positive ADT anomalies in the ETD, while the negative

anomalies cancel the positive anomalies in the R-ETD. As a result, the ADT gradient is favorable for the J2 deceleration as indicated by the thin blue line. **c** The negative PDO results in the positive ADT anomalies at the central North Pacific Ocean. If the anomalies overlap the R-ETD, they intensify the J2 as indicated by the thick blue line.

5. Summary and discussion

In this study, we explored the pathways of Kuroshio water into the J2 and ETD. We calculated the count function that measures the frequency of Kuroshio water pathways and identified the detailed pathways of Kuroshio water intrusion. As shown in Section 3.1, a large part of Kuroshio waters enters the ETD via the downstream region of KE (**Fig. 3**). At around the Shatzky Rise, the KE jet splits into the KENB and main KE. Some Kuroshio waters are trapped by the KENB, which directly confluence with J2. This is the most dominant pathway into the ETD, named *KENB route*. Another route is the *SAB route*. Some Kuroshio waters escape from the KENB owing to eddy activities, which are transported by the zonal flow associated with the SAB. As shown in **Fig. 4**, the SAB route confluences with the KENB route at the entrance of J2. Eddy transports also contribute to the Kuroshio water intrusion from the main KE. Although the KE jet flows eastward south of 35°N east of 153°E, eddies allow the Kuroshio waters to escape from the jet between 160°E and 170°E owing to the enhanced cross-stream eddy diffusivity in the downstream region of KE. With the aid of eddy activities, the Kuroshio waters flow northward and confluence with the J2. This route is named *KE-Eddy route*. Furthermore, the J1 jet also transports the Kuroshio water to the ETD without the confluence with J2, although its contribution is smaller than the other routes. Moreover, we confirmed that the SAB, KE-Eddy, and J1 routes are not available if temporal fluctuations of velocity fields are absent (**Fig. 5**) in Section 3.2, indicating that the eddies are essential for these routes. A schematic of the Kuroshio water intrusion is shown in **Fig. 20**.

To evaluate the roles of the Kuroshio water intrusion in the thermal condition of the ETD, we also analyzed the correlation coefficient of the Kuroshio water intrusion with the SST and turbulent heat flux. The results shown in **Fig. 6** indicate that the heat transport by the Kuroshio water intrusion regulates the local SST of the ETD. The heat transported by the Kuroshio water is released into the atmosphere, which may initiate atmospheric anomalous circulations. However, this relationship was broken in 2022. The SST has positive anomalies over the subarctic region after 2021 (**Fig. 7**) despite the weak amplitude of the Kuroshio water intrusion.

Furthermore, we discussed possible mechanisms of the decadal variation of the Kuroshio water intrusion. Although the Kuroshio waters intrude into the ETD via the downstream region of KE, the decadal variation of the Kuroshio intrusion is driven by the J2 intensity rather than the dynamical state of KE (**Fig. 8**). To explain the decadal variation of J2 intensity, we suggested novel remote and local mechanisms using the HEOF analyses (**Figs. 10‑15**). In the onset of the remote mechanism (**Fig. 19a**), the negative NPGO results in the positive anomalies in the Gulf of Alaska. At the same time, the positive PDO results in negative anomalies in the central North Pacific Ocean. As shown by the HEOF analyses, the positive anomalies associated with the negative NPGO propagate southwestward along the Alaska Peninsula, and finally reach the ETD (**Fig. 19b**). The negative ADT anomalies associated with the PDO also propagate westward as the baroclinic Rossby wave with slanting northeastward due to the phase speed difference by the latitude. As a result, the remotely forced positive anomalies are canceled by the positive PDO signals in the R-ETD, while the positive anomalies remain in the L-ETD, forming the favorable condition of J2 deceleration. The HEOF successfully separated these two different remote origins of the ADT anomalies and those propagations as two modes. The J2 acceleration during 2009‑2011, on the other hand, is due to the local mechanism, which is also separated as a HEOF mode. In this period, the ADT anomalies associated with the negative PDO overlap with the R-ETD, resulting in the favorable condition of the J2 acceleration (**Fig. 19c**). It should be noted that the proposed mechanisms in **Fig. 19** are primarily inferred from the case studies. As discussed in Section 4.3.3, the relationship between the J2 strength and the climate modes is complex. To validate how the climate modes control the J2 strength and Kuroshio water intrusion, longer-term data or simulations are required.

Although we discussed the decadal variation of the Kuroshio water intrusion and its impacts, the relative importance under global warming conditions should be discussed in future work. According to previous studies, the decadal variability of SST in the subarctic regions possibly migrates the North Pacific storm track and modulates the Aleutian Low (Taguchi et al. 2012). The oceanic processes including the Kuroshio water intrusion are considered to play essential roles in modulating the surface condition (e.g., Qiu et al. 2017; Kido et al. 2021; Nishikawa et al. 2021; Matsuta and Mitsudera 2023). However, global warming also causes the SST anomaly over the subarctic region as discussed in Section 4.1. Climate model experiments are necessary for evaluating the relative importance of the oceanic process under global warming conditions. In addition, long-term simulations are necessary to validate the proposed mechanisms in **Fig. 19**.

A challenge in conducting the simulations is that J1 and J2 are not resolved even in "eddy-resolving ocean general circulation models." The SST gradients in 2002 are shown in **Fig. 21** as an example. A comparison between the observation (**Fig. 21a**) and a hindcast of the ocean general circulation model named "OFES" with a resolution of $1/10° \times 1/10°$ (Sasaki et al. 2008) (**Fig. 21b**) indicates that an "eddy-resolving" model is insufficient for reproducing J1 and J2. In OFES, the SST front between $150°$E and $170°$E in the subarctic region is separated from the SST front associated with the SAB (see green contour), indicating the absence of J1 and J2. In the case of OFES with a resolution of $1/30° \times 1/30°$ (Sasaki and Klein 2012), the results are improved. It should be noted that the vertical resolution, the atmospheric forcing, and the mixing schemes are different from those of $1/10° \times 1/10°$ OFES, and therefore a simple comparison between the two models is difficult. According to **Fig. 21c**, J2 is not reproduced in this case although a northeastward flow exists in the region of $163°\mathrm{E} - 175°\mathrm{E}$, $39°\mathrm{N} - 42°\mathrm{N}$. On the other hand, J1 is reproduced. There exists the northeastward flow in the region of $150°\mathrm{E} - 160°\mathrm{E}$, $40°\mathrm{N} - 45°\mathrm{N}$, which is very consistent with the observation (see the same region in **Fig. 21a**). Therefore, to represent the air-sea interactions associated with J1 and J2, ocean models should be improved. In addition, a high-resolution atmospheric component is also necessary to respond to the steep SST gradients of J1 and J2. According to Tomita et al. (2011), the air-sea fluxes have fine-scale structures due to the SST gradient of J1, which is not resolved in the coarse models. The development of high-resolution climate models will help to establish the relationship between the J1 and J2 with the climate modes and global warming.

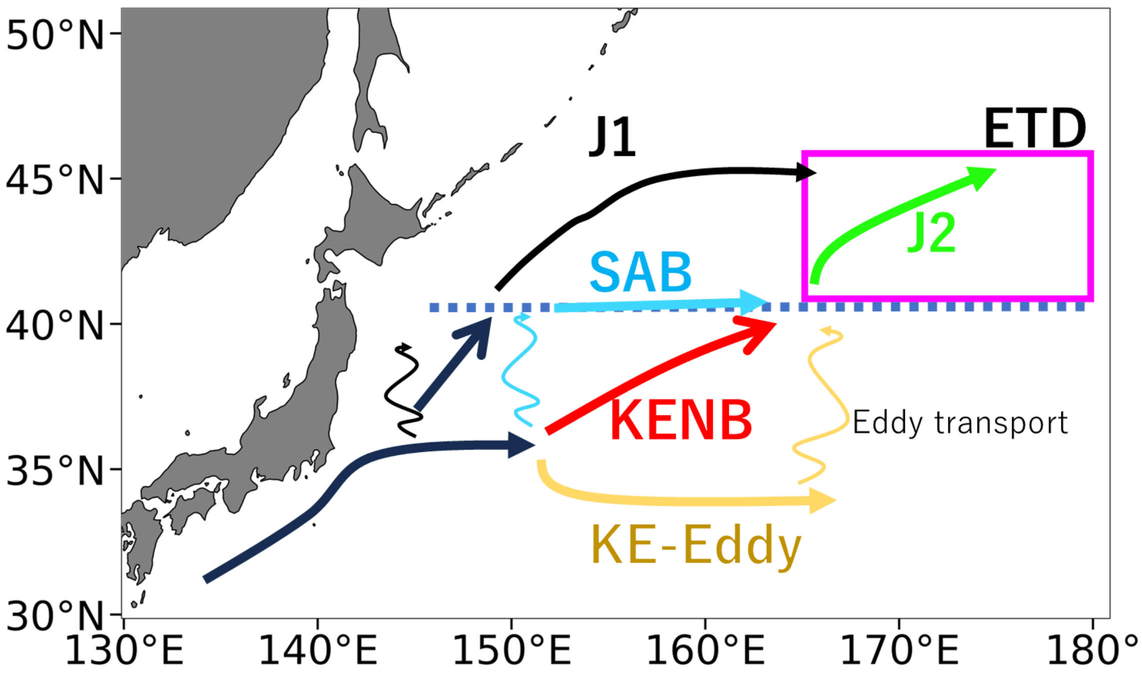

Fig. 20 Schematic of the Kuroshio water intrusion into ETD. The magenta rectangular region indicates the ETD and the dashed blue line indicates the SAB. The northward current associated with J2 is indicated by the green allow. The dominant pathway is the KENB route indicated by the red arrow, which directly connects with the J2 entrance. Some trajectories escape from the KENB owing to eddies indicated by the cyan-wavy arrow and are transported toward the J2 entrance by the zonal flow associated with the SAB. This route is the SAB route indicated by the cyan arrow. The KE-Eddy route indicated by the yellow arrow also contributes to the Kuroshio water intrusion. Some waters in the downstream region of KE are fluctuated northward by eddy transport, indicated by the yellow-wavy arrow at around 162°E and enter the ETD. In addition, the J1 route also contributes to the Kuroshio water intrusion into the ETD. Eddies also enhance the Kuroshio water intrusion into the J1 indicated by the black-wavy arrow.

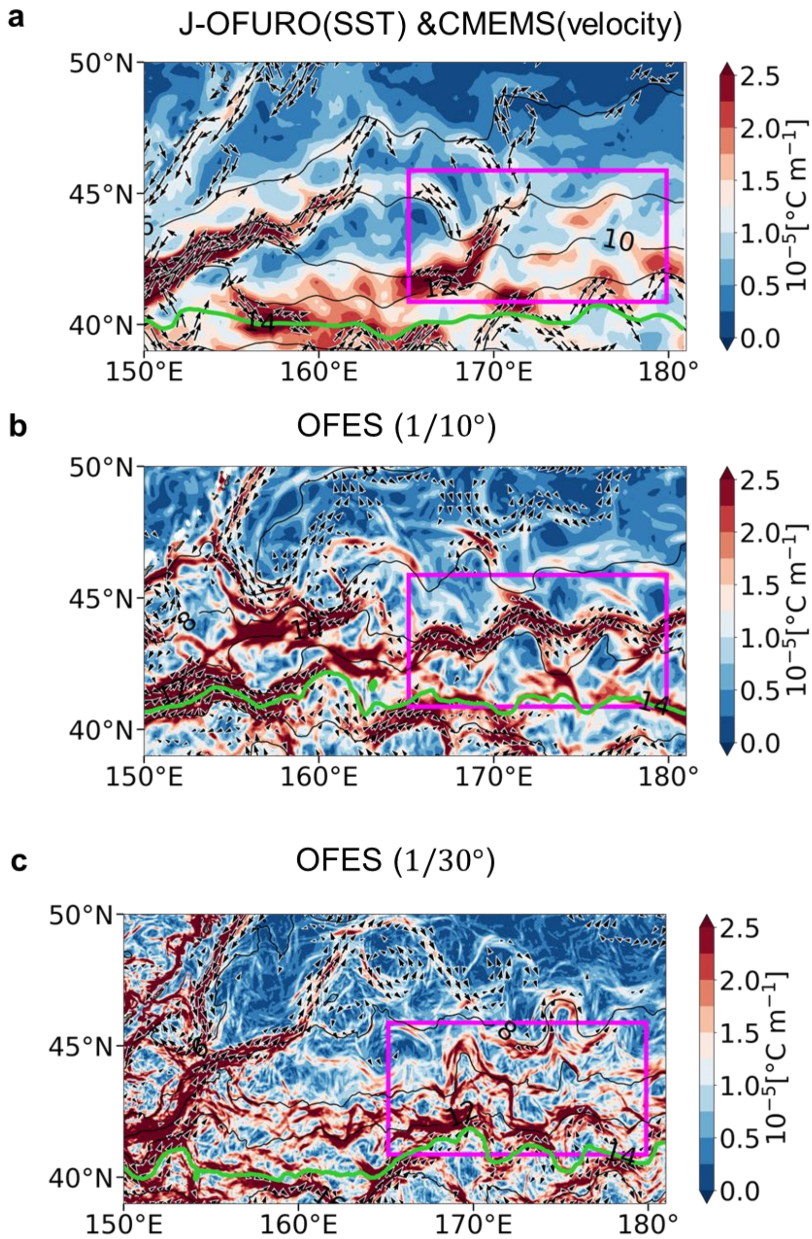

Fig. 21. Same as **Fig. 1b** but averaged in 2002 for **a** the observation, **b** OFES with a resolution of $1/10° \times 1/10°$, and **c** OFES with a resolution of $1/30° \times 1/30°$. Velocity vectors whose speeds are less than 10 cm s^{-1} are masked.

Appendix: An introduction to the HEOF analysis

Here, we briefly introduce the HEOF following Barnett (1983). Let $\mathbf{q}_t = \{q(\boldsymbol{x}_k, t)\}^T{}_{k=1,\ldots,N_x}$ be the vector whose entry is a scaler value q at time t and at the position $\boldsymbol{x}_k$. Here, $N_{\boldsymbol{x}}$ is the total number of grids and $\cdot^T$ indicates the transpose of a vector. The vector can be written with the Fourier representation as follows:

$$\mathbf{q}_t = \sum_{\omega} (\mathbf{a}(\omega)\cos\omega t + \mathbf{b}(\omega)\sin\omega t), \tag{A1}$$

where ω is the frequency, and $\mathbf{a}(\omega)$ and $\mathbf{b}(\omega)$ are vector Fourier coefficients. The Hilbert transform, $\mathcal{H}(\cdot)$ of $\mathbf{q}_t$ corresponds to a phase shift by $1/2\pi$ in time:

$$\mathcal{H}(\mathbf{q}_t) = \sum_{\omega} (\mathbf{b}(\omega)\cos\omega t - \mathbf{a}(\omega)\sin\omega t). \tag{A2}$$

Now, we define the new complex field, $\tilde{\mathbf{q}}_t$ as follows:

$$\tilde{\mathbf{q}}_t = \mathbf{q}_t + i\mathcal{H}(\mathbf{q}_t), \tag{A3}$$

where i is the imaginary unit. The new field can be represented as a waveform,

$$\tilde{\mathbf{q}}_t = \sum_{\omega} \mathbf{c}(\omega)\mathrm{e}^{-i\omega t}, \tag{A4}$$

where $\mathbf{c}(\omega) = \mathbf{a}(\omega) + i\mathbf{b}(\omega)$ and the real part of $\tilde{\mathbf{q}}_t$ is equal to $\mathbf{q}_t$. In the HEOF, we seek the eigenvectors of the time-averaged Hermitian covariance matrix, C,

$$C = \frac{1}{N_t}\sum_{n=1}^{N_t} \tilde{\mathbf{q}}^*_{t_n}\tilde{\mathbf{q}}_{t_n}, \tag{A5}$$

where $\cdot^*$ indicates the adjoint of the complex matrix, t_n is the time when $\tilde{\mathbf{q}}_t$ is observed, and N_t is the length of the time series. Since C is the Hermitian, it possesses real eigenvalues and complex eigenvectors, $B_n(\boldsymbol{x}_k)$. Using the eigenvectors, we decompose the field as follows

$$\tilde{\mathbf{q}}(\mathbf{x}_k, t) = \sum_{m=1}^{M} A_m(t)B^*_m(\mathbf{x}_k), \tag{A6}$$

where A_m is the *m-th* time-dependent principal component given by

$$A_m(t) = \sum_{k=1}^{N_x} \tilde{\mathbf{q}}(\mathbf{x}_k, t)B_m(\boldsymbol{x}_k). \tag{A7}$$

As in the conventional EOF, the eigenvalue associated with B_m corresponds to the fraction of total variance explained by the *m-th* mode. We call the real part of each HEOF mode, Re $(A_m B_m^*)$ as the reconstructed field from the *m-th* mode, where $\mathrm{Re}(\cdot)$ returns the real part of complex values.

From the HEOF modes, we obtain the spatial amplitude, S_m and relative phase, θ_m of the *m-th* mode

$$S_m(\mathbf{x}_k) = \left[B_m(\mathbf{x}_k) B_m^{*\,T}(\mathbf{x}_k)\right]^{\frac{1}{2}}, \quad \text{(A8)}$$

and

$$\theta_m(\mathbf{x}_k) = \arctan\left(\frac{\mathrm{Im}\left(B_m(\mathbf{x}_k)\right)}{\mathrm{Re}\left(B_m(\mathbf{x}_k)\right)}\right), \quad \text{(A9)}$$

where Im $(\cdot)$ returns the imaginary part of complex values. The amplitude measures the spatial distribution of intensity of the *m-th* mode. Especially, the amplitude has large values along waveguides if the mode is represented as a single wave. As for the relative phase, the spatial derivative of the phase corresponds to the local wave number, and thereby the spatial change of the phase function gives the direction of wave propagation.

Similarly, we also obtain the temporal amplitude, R_m and phase, ϕ_m of the *m-th* mode:

$$R_m(t) = [A_m(t) A_m^*(t)]^{\frac{1}{2}}, \quad \text{(A10)}$$

and

$$\phi_m(t) = \arctan\left(\frac{\mathrm{Im}\,(A_m(t))}{\mathrm{Re}\,(A_m(t))}\right). \quad \text{(A11)}$$

The temporal amplitude measures the temporal variability of the *m-th* mode, and the time derivative of the phase corresponds to the temporal frequency of the mode. If the wave has a simple sinusoidal form, $D\sin(\omega_0 t)$ with a constant amplitude, D and a constant frequency ω_0, the temporal amplitude is always D and the phase is equal to $\omega_0 t$. A more detailed introduction to the HEOF is found in a comprehensive review by Hannachi et al. (2007). In this work, the HEOF code is implemented using a Python library for EOF analyses, “xeofs” (Rieger and Levang 2024).

Acknowledgment

Takuro Matsuta was supported by JSPS Grant-in-Aid for JSPS Fellows No. 22J00651 and JSPS Grant-in-Aid No. 24K17120. Humio Mitsudera was supported by JSPS Grant-in-Aid No. 19H05701 and 21H01154. Toru Miyama was supported by JSPS Grant-in-Aid No. 20H01968 and 19H05697. Hiroyuki Tomita was supported by JSPS Grant-in-Aid No. 19H05696, 23H01239, and JAXA GCOM RA. Takuro Matsuta thanks Hideharu Sasaki. He kindly provided the data of OFES with the resolution of $1/30^\circ \times 1/30^\circ$.

Data Availability

The current data are available at the Website: https://data.marine.copernicus.eu/product/SEALEVEL_GLO_PHY_CLIMATE_L4_MY_008_057/description. The J-OFURO3 v1.2 data will be available at https://doi.org/10.20783/DIAS.667. The data of OFES with the resolution of $1/10^\circ \times 1/10^\circ$ are available at https://www.jamstec.go.jp/ofes/ofes.html. The data of OFES with the resolution of $1/30^\circ \times 1/30^\circ$ are available upon reasonable request.

REFERENCES

Aoki, K., A. Kubokawa, R. Furue, and H. Sasaki, 2016: Influence of Eddy Momentum Fluxes on the Mean Flow of the Kuroshio Extension in a 1/10° Ocean General Circulation Model. *J Phys Oceanogr*, **46**, 2769–2784, https://doi.org/10.1175/JPO-D-16-0021.1.

Barnett, T. P., 1983: Interaction of the Monsoon and Pacific Trade Wind System at Interannual Time Scales Part I: The Equatorial Zone. *Mon Weather Rev*, **111**, 756–773, https://doi.org/10.1175/1520-0493(1983)111<0756:IOTMAP>2.0.CO;2.

Chen, R., G. R. Flierl, and C. Wunsch, 2014a: A description of local and nonlocal eddy-mean flow interaction in a global eddy-permitting state estimate. *J Phys Oceanogr*, **44**, 2336–2352, https://doi.org/10.1175/JPO-D-14-0009.1.

——, J. L. McClean, S. T. Gille, and A. Griesel, 2014b: Isopycnal eddy diffusivities and critical layers in the Kuroshio extension from an eddying ocean model. *J Phys Oceanogr*, **44**, 2191–2211, https://doi.org/10.1175/JPO-D-13-0258.1.

Hannachi, A., I. T. Jolliffe, and D. B. Stephenson, 2007: Empirical orthogonal functions and related techniques in atmospheric science: A review. *International Journal of Climatology*, **27**, 1119–1152, https://doi.org/10.1002/joc.1499.

Horel, J. D., 1984: Complex Principal Component Analysis: Theory and Examples. *Journal of Climate and Applied Meteorology*, **23**, 1660–1673, https://doi.org/10.1175/1520-0450(1984)023<1660:CPCATA>2.0.CO;2.

Hurlburt, H. E., and E. J. Metzger, 1998: Bifurcation of the kuroshio extension at the shatsky rise. *J Geophys Res Oceans*, **103**, 7549–7566, https://doi.org/10.1029/97jc02723.

Isoguchi, O., H. Kawamura, and E. Oka, 2006: Quasi-stationary jets transporting surface warm waters across the transition zone between the subtropical and the subarctic gyres in the North Pacific. *J Geophys Res Oceans*, **111**, https://doi.org/10.1029/2005JC003402.

Joh, Y., T. L. Delworth, A. T. Wittenberg, X. Yang, A. Rosati, N. C. Johnson, and L. Jia, 2023: The role of upper-ocean variations of the Kuroshio-Oyashio Extension in seasonal-to-decadal air-sea heat flux variability. *NPJ Clim Atmos Sci*, **6**, https://doi.org/10.1038/s41612-023-00453-9.

Kawakami, Y., H. Nakano, L. S. Urakawa, T. Toyoda, K. Aoki, and N. Usui, 2023: Northward shift of the Kuroshio Extension during 1993–2021. *Sci Rep*, **13**, https://doi.org/10.1038/s41598-023-43009-w.

Kida, S., and Coauthors, 2015: Oceanic fronts and jets around Japan: a review. *J Oceanogr*, **71**, 469–497, https://doi.org/10.1007/s10872-015-0283-7.

Kido, S., M. Nonaka, and Y. Tanimoto, 2021: Impacts of Salinity Variation on the Mixed-Layer Processes and Sea Surface Temperature in the Kuroshio-Oyashio Confluence Region. *J Geophys Res Oceans*, **126**, https://doi.org/10.1029/2020JC016914.

Kwon, Y. O., M. A. Alexander, N. A. Bond, C. Frankignoul, H. Nakamura, B. Qiu, and L. A. Thompson, 2010: Role of the gulf Stream and Kuroshio-Oyashio systems in large-scale atmosphere-ocean interaction: A review. *J Clim*, **23**, 3249–3281, https://doi.org/10.1175/2010JCLI3343.1.

Levine, E. R., and W. B. White, 1983: Bathymetric influences upon the character of North Pacific Fronts, 1976–1980. *J Geophys Res Oceans*, **88**, 9617–9625, https://doi.org/10.1029/JC088iC14p09617.

Di Lorenzo, E., and Coauthors, 2008: North Pacific Gyre Oscillation links ocean climate and ecosystem change. *Geophys Res Lett*, **35**, https://doi.org/10.1029/2007GL032838.

Ma, X., and Coauthors, 2015: Distant Influence of Kuroshio Eddies on North Pacific Weather Patterns? *Sci Rep*, **5**, https://doi.org/10.1038/srep17785.

——, and Coauthors, 2016: Western boundary currents regulated by interaction between ocean eddies and the atmosphere. *Nature*, **535**, 533–537, https://doi.org/10.1038/nature18640.

Mantua, N. J., S. R. Hare, Y. Zhang, J. M. Wallace, and R. C. Francis, 1997: A Pacific Interdecadal Climate Oscillation with Impacts on Salmon Production. *Bull Am Meteorol Soc*, **78**, 1069–1079, https://doi.org/10.1175/1520-0477(1997)078<1069:APICOW>2.0.CO;2.

Matsuta, T., and Y. Masumoto, 2021: Modified View of Energy Budget Diagram and Its Application to the Kuroshio Extension Region. *J Phys Oceanogr*, **51**, 1163–1175, https://doi.org/10.1175/JPO-D-20-0124.1.

——, and H. Mitsudera, 2023: Kuroshio water intrusion into the subarctic region in the western North Pacific Ocean and analyses of the Lagrangian coherent structure. *J Oceanogr*, https://doi.org/10.1007/s10872-023-00696-3.

Mitsudera, H., and Coauthors, 2018: Low ocean-floor rises regulate subpolar sea surface temperature by forming baroclinic jets. *Nat Commun*, **9**, 1–11, https://doi.org/10.1038/s41467-018-03526-z.

Miyama, T., S. Minobe, and H. Goto, 2021: Marine Heatwave of Sea Surface Temperature of the Oyashio Region in Summer in 2010–2016. *Front Mar Sci*, **7**, https://doi.org/10.3389/fmars.2020.576240.

Mizuno, K., and W. B. White, 1983: Annual and Interannual Variability in the Kuroshio Current System. *J Phys Oceanogr*, **13**, 1847–1867, https://doi.org/10.1175/1520-0485(1983)013<1847:AAIVIT>2.0.CO;2.

Nakamura, H., T. Sampe, Y. Tanimoto, and A. Shimpo, 2004: Observed Associations Among Storm Tracks, Jet Streams and Midlatitude Oceanic Fronts. 329–345.

Nishikawa, H., and Coauthors, 2021: Surface water pathways in the subtropical–subarctic frontal zone of the western North Pacific. *Prog Oceanogr*, **199**, 102691, https://doi.org/10.1016/j.pocean.2021.102691.

Niu, Z., Z. Chen, W. Yu, H. Guo, R. Zhu, and X. Zhang, 2024: Temporal and spatial variations in squid jigging catch efficiency in the Oyashio Extension region. *Fish Oceanogr*, https://doi.org/10.1111/fog.12692.

Nonaka, M., H. Nakamura, Y. Tanimoto, T. Kagimoto, and H. Sasaki, 2006: Decadal Variability in the Kuroshio–Oyashio Extension Simulated in an Eddy-Resolving OGCM. *J Clim*, **19**, 1970–1989, https://doi.org/10.1175/JCLI3793.1.

Ogawa, F., H. Nakamura, K. Nishii, T. Miyasaka, and A. Kuwano-Yoshida, 2012: Dependence of the climatological axial latitudes of the tropospheric westerlies and storm tracks on the latitude of an extratropical oceanic front. *Geophys Res Lett*, **39**, https://doi.org/10.1029/2011GL049922.

Oyaizu, H., S. Suyama, D. Ambe, S. ichi Ito, and S. Itoh, 2022: Modeling the growth, transport, and feeding migration of age-0 Pacific saury Cololabis saira. *Fisheries Science*, **88**, 131–147, https://doi.org/10.1007/s12562-021-01578-7.

Qiu, B., and S. Chen, 2010: Eddy-mean flow interaction in the decadally modulating Kuroshio Extension system. *Deep Sea Res 2 Top Stud Oceanogr*, **57**, 1098–1110, https://doi.org/10.1016/j.dsr2.2008.11.036.

——, ——, and N. Schneider, 2017: Dynamical links between the decadal variability of the Oyashio and Kuroshio Extensions. *J Clim*, **30**, 9591–9605, https://doi.org/10.1175/JCLI-D-17-0397.1.

——, ——, ——, E. Oka, and S. Sugimoto, 2021: On the reset of the wind-forced decadal kuroshio extension variability in late 2017. *J Clim*, **33**, 10813–10828, https://doi.org/10.1175/JCLI-D-20-0237.1.

Qiu, B. O., 2003: *Kuroshio Extension Variability and Forcing of the Pacific Decadal Oscillations: Responses and Potential Feedback.*

Rasmusson, E. M., P. A. Arkin, W.-Y. Chen, and J. B. Jalickee, 1981: Biennial Variations in Surface Temperature over the United States as Revealed by Singular Decomposition. *Mon Weather Rev*, **109**, 587–598, https://doi.org/10.1175/1520-0493(1981)109<0587:BVISTO>2.0.CO;2.

Rieger, N., and S. J. Levang, 2024: xeofs: Comprehensive EOF analysis in Python with xarray. *J Open Source Softw*, **9**, 6060, https://doi.org/10.21105/joss.06060.

Sainz-Trapaga, S. M., G. J. Goni, and T. Sugimoto, 2001: Identification of the Kuroshio Extension, its Bifurcation and Northern Branch from altimetry and hydrographic data during October 1992 - August 1999: Spatial and temporal variability. *Geophys Res Lett*, **28**, 1759–1762, https://doi.org/10.1029/2000GL012323.

Sasaki, H., and P. Klein, 2012: SSH Wavenumber Spectra in the North Pacific from a high-resolution: Realistic simulation. *J Phys Oceanogr*, **42**, 1233–1241, https://doi.org/10.1175/JPO-D-11-0180.1.

——, M. Nonaka, Y. Masumoto, Y. Sasai, H. Uehara, and H. Sakuma, 2008: An Eddy-Resolving Hindcast Simulation of the Quasiglobal Ocean from 1950 to 2003 on the Earth Simulator. *High Resolution Numerical Modelling of the Atmosphere and Ocean*, Springer New York, 157–185.

Storto, A., and C. Yang, 2024: Acceleration of the ocean warming from 1961 to 2022 unveiled by large-ensemble reanalyses. *Nat Commun*, **15**, https://doi.org/10.1038/s41467-024-44749-7.

Sugimoto, S., 2014: Influence of SST anomalies on winter turbulent heat fluxes in the eastern Kuroshio-Oyashio confluence region. *J Clim*, **27**, 9349–9358, https://doi.org/10.1175/JCLI-D-14-00195.1.

Taguchi, B., S. P. Xie, N. Schneider, M. Nonaka, H. Sasaki, and Y. Sasai, 2007: Decadal variability of the Kuroshio Extension: Observations and an eddy-resolving model hindcast. *J Clim*, **20**, 2357–2377, https://doi.org/10.1175/JCLI4142.1.

——, H. Nakamura, M. Nonaka, and S. P. Xie, 2009: Influences of the Kuroshio/Oyashio extensions on air-sea heat exchanges and storm-track activity as revealed in regional atmospheric model simulations for the 2003/04 cold season. *J Clim*, **22**, 6536–6560, https://doi.org/10.1175/2009JCLI2910.1.

——, ——, ——, N. Komori, A. Kuwano-Yoshida, K. Takaya, and A. Goto, 2012: Seasonal evolutions of atmospheric response to decadal SST anomalies in the North Pacific subarctic frontal zone, observations and a coupled model simulation. *J Clim*, **25**, 111–139, https://doi.org/10.1175/JCLI-D-11-00046.1.

Takahashi, N., T. Hayasaka, A. Manda, and N. Schneider, 2020: Impact of the Oyashio Extension SST Front on Synoptic Variability of Oceanic Low-Level Cloud in Summertime Based on WRF Numerical Simulation. *Journal of Geophysical Research: Atmospheres*, **125**, https://doi.org/10.1029/2020JD032518.

Tanimoto, Y., H. Nakamura, T. Kagimoto, and S. Yamane, 2003: An active role of extratropical sea surface temperature anomalies in determining anomalous turbulent heat flux. *J Geophys Res Oceans*, **108**, https://doi.org/10.1029/2002jc001750.

Tomita, H., S. Kouketsu, E. Oka, and M. Kubota, 2011: Locally enhanced wintertime air-sea interaction and deep oceanic mixed layer formation associated with the subarctic front in the North Pacific. *Geophys Res Lett*, **38**, https://doi.org/10.1029/2011GL049902.

——, T. Hihara, S. Kako, M. Kubota, and K. Kutsuwada, 2019: An introduction to J-OFURO3, a third-generation Japanese ocean flux data set using remote-sensing observations. *J Oceanogr*, **75**, 171–194, https://doi.org/10.1007/s10872-018-0493-x.

Wagawa, T., S. I. Ito, Y. Shimizu, S. Kakehi, and D. Ambe, 2014: Currents associated with the quasi-stationary jet separated from the Kuroshio extension. *J Phys Oceanogr*, **44**, 1636–1653, https://doi.org/10.1175/JPO-D-12-0192.1.

Xie, S. P., 2004: Satellite observations of cool ocean-atmosphere interaction. *Bull Am Meteorol Soc*, **85**, https://doi.org/10.1175/bams-85-2-195.

Yang, H., and Coauthors, 2020: Poleward Shift of the Major Ocean Gyres Detected in a Warming Climate. *Geophys Res Lett*, **47**, https://doi.org/10.1029/2019GL085868.

Yang, Y., and X. S. Liang, 2016: The instabilities and multiscale energetics underlying the mean-interannual-eddy interactions in the Kuroshio Extension region. *J Phys Oceanogr*, **46**, 1477–1494, https://doi.org/10.1175/JPO-D-15-0226.1.

——, ——, and H. Sasaki, 2021: Vertical coupling and dynamical source for the intraseasonal variability in the deep Kuroshio Extension. *Ocean Dyn*, https://doi.org/10.1007/s10236-021-01482-9.

Yasuda, T., and Y. Kitamura, 2003: Long-Term Variability of North Pacific Subtropical Mode Water in Response to Spin-Up of the Subtropical Gyre. *J Oceanogr*, **59**, 279, https://doi.org/https://doi.org/10.1023/A:1025507725222.